

**Repository of the Max Delbrück Center for Molecular Medicine (MDC)
in the Helmholtz Association**

<https://edoc.mdc-berlin.de/20923/>

Virus-induced senescence is driver and therapeutic target in COVID-19

Lee S., Yu Y., Trimpert J., Benthani F., Mairhofer M., Richter-Pechanska P., Wyler E., Belenki D., Kaltenbrunner S., Pammer M., Kausche L., Firsching T.C., Dietert K., Schotsaert M., Martínez-Romero C., Singh G., Kunz S., Niemeyer D., Ghanem R., Salzer H.J.F., Paar C., Mülleder M., Uccellini M., Michaelis E.G., Khan A., Lau A., Schönlein M., Habringer A., Tomasits J., Adler J.M., Kimeswenger S., Gruber A.D., Hoetzenecker W., Steinkellner H., Purfuerst B., Motz R., Di Pierro F., Lamprecht B., Osterrieder N., Landthaler M., Drosten C., García-Sastre A., Langer R., Ralser M., Eils R., Reimann M., Fan D.N.Y., Schmitt C.A.

This is the final version of the accepted manuscript. The original article has been published in final edited form in:

Nature
2021 NOV 11 ; 599: 283-289
2021 SEP 13 (first published online: final version)
doi: [10.1038/s41586-021-03995-1](https://doi.org/10.1038/s41586-021-03995-1)
URL: <https://www.nature.com/articles/s41586-021-03995-1>

Publisher: [Nature Research](#) (Springer Nature)

Copyright © 2021, The Author(s), under exclusive licence to Springer Nature Limited

Publisher's Notice

This version of the article has been accepted for publication, after peer review (when applicable) and is subject to Springer Nature's [AM terms of use](#), but is not the Version of Record and does not reflect post-acceptance improvements, or any corrections. The Version of Record is available online at <https://doi.org/10.1038/s41586-021-03995-1>.

1 **Virus-induced senescence is driver and therapeutic target in** 2 **COVID-19**

3 Soyoung Lee^{1-3*}, Yong Yu^{4*}, Jakob Trimper⁵, Fahad Benthani⁴, Mario Mairhofer⁴, Paulina
4 Richter-Pechanska¹, Emanuel Wyler², Dimitri Belenki^{1,2}, Sabine Kaltenbrunner⁴, Maria
5 Pammer⁴, Lea Kausche^{1,6}, Theresa C. Firsching⁷, Kristina Dietert^{7,8}, Michael Schotsaert^{9,10},
6 Carles Martínez-Romero^{9,10}, Gagandeep Singh^{9,10}, Séverine Kunz², Daniela Niemeyer¹¹, Riad
7 Ghanem⁶, Helmut J. F. Salzer¹², Christian Paar¹³, Michael Mülleder¹⁴, Melissa Uccellini^{9,10†},
8 Edward G. Michaelis¹⁵, Amjad Khan¹⁶, Andrea Lau¹, Martin Schönlein^{1,17}, Anna Habringer¹³,
9 Josef Tomasits¹³, Julia M. Adler⁵, Susanne Kimeswenger⁴, Achim D. Gruber⁷, Wolfram
10 Hoetzenecker^{4,18}, Herta Steinkellner¹⁹, Bettina Purfürst², Reinhard Motz²⁰, Francesco Di
11 Pierro^{21,22}, Bernd Lamprecht^{4,12}, Nikolaus Osterrieder^{5,23}, Markus Landthaler², Christian
12 Drosten¹¹, Adolfo García-Sastre^{9,10,24,25}, Rupert Langer^{4,20}, Markus Ralser^{13,26}, Roland Eils²⁷,
13 Maurice Reimann¹, Dorothy N. Y. Fan^{1,3}, and Clemens A. Schmitt^{1-4,6}

14

15 ¹Charité - Universitätsmedizin and Berlin Institute of Health (BIH), Medical Department of
16 Hematology, Oncology and Tumor Immunology, and Molekulares Krebsforschungszentrum –
17 MKFZ, Campus Virchow Klinikum, Augustenburger Platz 1, 13353 Berlin, Germany

18 ²Max-Delbrück-Center for Molecular Medicine in the Helmholtz Association, Robert-Rössle-
19 Straße 10, 13125 Berlin, Germany

20 ³Deutsches Konsortium für Translationale Krebsforschung (German Cancer Consortium),
21 Partner site Berlin, Germany

22 ⁴Johannes Kepler University, Altenbergerstraße 69, 4040 Linz, Austria

23 ⁵Institute of Virology, Freie Universität Berlin, Robert von Ostertag-Straße 7-13, 14163 Berlin,
24 Germany

25 ⁶Kepler University Hospital, Department of Hematology and Oncology, Krankenhausstraße 9,
26 4021 Linz, Austria

27 ⁷Institute of Veterinary Pathology, Freie Universität Berlin, Robert-von-Ostertag-Straße 15,
28 14163 Berlin, Germany

29 ⁸Veterinary Centre for Resistance Research, Freie Universität Berlin, Robert-von-Ostertag-
30 Straße 8, 14163 Berlin, Germany

31 ⁹Department of Microbiology, Icahn School of Medicine at Mount Sinai, 1 Gustave L. Levy
32 Place, New York, NY 10029, USA

33 ¹⁰Global Health and Emerging Pathogens Institute, Icahn School of Medicine at Mount Sinai,
34 1 Gustave L. Levy Place, New York, NY 10029, USA

35 ¹¹Charité - Universitätsmedizin, Institute of Virology; German Center for Infection Research
36 (DZIF), Charitéplatz 1, 10117 Berlin, Germany

37 ¹²Kepler University Hospital, Department of Pulmonology, Krankenhausstraße 9, 4021 Linz,
38 Austria

39 ¹³Kepler University Hospital, Laboratory Medicine, Krankenhausstraße 9, 4021 Linz, Austria

40 ¹⁴Charité - Universitätsmedizin, Department of Biochemistry, Charitéplatz 1, 10117 Berlin,
41 Germany

42 ¹⁵Charité - Universitätsmedizin, Institute of Pathology, Charitéplatz 1, 10117 Berlin, Germany

43 ¹⁶Department of Chemistry, University of Oxford, Mansfield Road, OX1 3TA, Oxford, UK

44 ¹⁷Department of Oncology, Hematology and Bone Marrow Transplantation with Section of
45 Pneumology, University Medical Center Hamburg-Eppendorf, Martinistraße 52, 20251
46 Hamburg, Germany

47 ¹⁸Kepler University Hospital, Department of Dermatology, Krankenhausstraße 9, 4021 Linz,
48 Austria

49 ¹⁹Department of Applied Genetics and Cell Biology, University of Natural Resources and Life
50 Sciences, Muthgasse 18, 1190 Vienna, Austria

51 ²⁰Kepler University Hospital, Institute of Pathology, Krankenhausstraße 9, 4021 Linz, Austria

52 ²¹Scientific & Research Department, Velleja Research, Viale Lunigiana, 23, 20125 Milan, Italy

53 ²²Digestive Endoscopy, Fondazione Poliambulanza, Via Leonida Bissolati 57, 25124 Brescia,
54 Italy

55 ²³Department of Infectious Diseases and Public Health, City University of Hong Kong,
56 Kowloon Tong, Hong Kong

57 ²⁴Department of Medicine, Division of Infectious Diseases, Icahn School of Medicine at Mount
58 Sinai, 1 Gustave L. Levy Place, New York, NY 10029, USA

59 ²⁵The Tisch Cancer Institute, Icahn School of Medicine at Mount Sinai, 1 Gustave L. Levy
60 Place, New York, NY 10029, USA

61 ²⁶The Molecular Biology of Metabolism Laboratory, The Francis Crick Institute, London NW1
62 1AT, UK

63 ²⁷Center for Digital Health, Berlin Institute of Health (BIH) and Charité - Universitätsmedizin
64 Berlin, Anna-Louisa-Karsch-Straße 2, 10178 Berlin, Germany

65

66 *) These authors contributed equally

67 †) Current address: Regeneron Pharmaceuticals Inc., Tarrytown, New York, NY 10591, USA.

68

69 **Derailed cytokine and immune cell networks account for organ damage and clinical**
70 **severity of COVID-19¹⁻⁴. Here we show that SARS-CoV-2, like other viruses, evokes**
71 **cellular senescence as a primary stress response in infected cells. Virus-induced**
72 **senescence (VIS) is indistinguishable from other forms of cellular senescence and**
73 **accompanied by a senescence-associated secretory phenotype (SASP), composed of pro-**
74 **inflammatory cytokines, extracellular matrix-active factors and pro-coagulatory**
75 **mediators⁵⁻⁷. COVID-19 patients displayed markers of senescence in their airway mucosa**
76 ***in situ* and elevated serum levels of SASP factors. Mirroring COVID-19 hallmark features**
77 **such as macrophage and neutrophil infiltration, endothelial damage and widespread**
78 **thrombosis in affected lung tissue^{1,8,9}, *in vitro*-assays demonstrated macrophage activation**
79 **with SASP-reminiscent secretion, complement lysis and SASP-amplifying secondary**
80 **senescence of endothelial cells, neutrophil extracellular trap (NET) formation as well as**
81 **activation of platelets and the clotting cascade in response to supernatant of VIS cells,**
82 **including SARS-CoV-2-induced senescence. Senolytics such as Navitoclax and**
83 **Dasatinib/Quercetin selectively eliminated VIS cells, mitigated COVID-19-reminiscent**
84 **lung disease and reduced inflammation in SARS-CoV-2-driven hamster and mouse**
85 **models. Our findings mark VIS as pathogenic trigger of COVID-19-related cytokine**
86 **escalation and organ damage, and suggest senolytic targeting of virus-infected cells as a**
87 **novel treatment option against SARS-CoV-2 and perhaps other viral infections.**

88

89 The pandemic human pathogenic SARS-CoV-2 coronavirus causes upper respiratory infections
90 and subsequently COVID-19 lung disease that may get further complicated by septic multi-
91 organ failure and comes with significant mortality^{10,11}. Escalating immune activation with
92 massive cytokine release seems to drive severe COVID-19¹⁻³, possibly more than the virus

93 infection itself. Mechanisms of viral entry – primarily *via* interaction of CoV-2 spike protein S
94 with the host cell receptor ACE2 (angiotensin-converting enzyme 2) – and consecutive steps of
95 RNA replication, virus assembly and budding represent therapeutic targets^{12,13}. While anti-
96 inflammatory drugs are clinically being used or currently tested with mixed results^{14,15}, more
97 comprehensive and causal measurements to control the cytokine storm are needed.

98 Viral entry reflects a major cellular insult, and evokes profound biological changes in infected
99 host cells – potentially leading to cellular senescence as a virus-triggered state switch^{16,17}, with
100 controversial impact on virus propagation^{18,19}. Senescence is also acutely stress-induced by
101 activated oncogenes (OIS) or DNA-damaging cancer therapy, and physiologically occurs in
102 embryonic development, wound healing and ageing⁶. Little is known about systemic
103 ramifications of cellular senescence as an anti-viral host defense. We hypothesize here that
104 cellular senescence with its massive SASP, largely composed of pro-inflammatory cytokines,
105 matrix-degrading proteases and pro-coagulatory factors⁵⁻⁷, underlies the cytokine storm,
106 macrophage activation, NET formation, endothelialitis and widespread pulmonary thrombosis
107 frequently observed in COVID-19 patients^{1,8,9}.

108

109 **Properties of virus-induced senescence**

110 We first tested signs of senescence in human diploid fibroblast (HDF) models exposed to high-
111 titer retrovirus. At day 5 post infection (p.i.), most of the cells presented with a senescence-
112 typical flattened, enlarged morphology, stained positive in the senescence-associated β -
113 galactosidase (SA- β -gal) assay²⁰, exhibited DAPI (4',6-diamidin-2-phenylindol)-dense
114 chromatin reminiscent of senescence-associated heterochromatin foci (SAHF)²¹, and
115 overexpressed p16^{INK4a}, an inhibitor of cyclin-dependent kinases (CDK) 4 and 6, in the nucleus

116 (Fig. 1a, Extended Data Fig. 1a). Gene set enrichment analyses (GSEA) of HDF RNA
117 sequencing (RNA-seq) datasets found senescence- and SASP-related gene ontology (GO) terms
118 skewed towards the VIS state, and to overlap with the OIS state of the very same cells in Ras-
119 induced senescence (Fig. 1b). Further underlining the context-overarching role of a senescent
120 stress response, GSEA retrieved host responses to viral infection in OIS (Extended Data
121 Fig. 1b). Specific analyses of VIS-associated expression changes by quantitative RT-PCR
122 (qRT-PCR) found senescence-typical transcriptional changes^{21,22} in VIS (Fig. 1c, Extended
123 Data Fig. 1c). Notably, lower virus titers did not evoke a senescent cell-cycle arrest, as aimed
124 for in retro- or lentivirus-assisted gene transfer experiments (Extended Data Fig. 1d). Multiplex
125 protein analysis found VIS cells to secrete a plethora of SASP factors, many of them *bona fide*
126 NF- κ B targets^{23,24} (Fig. 1d). Importantly, these responses depended on senescence-essential
127 gene activities: HDF expressing the H3K9me3-active demethylase JMJD2C or engineered with
128 a small hairpin stably knocking down p53 (*shp53*) to genetically disable OIS^{22,25}, as well as
129 mouse embryo fibroblasts (MEF) without intact *p53* alleles failed to enter VIS, and lacked
130 senescence-typical changes by qRT-PCR and multiplex secretome analyses (Fig. 1e, Extended
131 Data Fig. 1e-g). Upon viral infection, only VIS-capable cells presented with cGAS/STING
132 activation (Extended Data Fig. 1h), a SASP-underlying interferon response-driving
133 cytoplasmic DNA sensor²⁶. Importantly, blocking retroviral replication *via* the reverse
134 transcriptase inhibitor Azidothymidine prevented VIS, and blunted cGAS/STING activation
135 (Extended Data Fig. 1i, j). cGAS/STING-mediated phospho-activation of the interferon
136 regulatory factor IRF3²⁷, the NF- κ B transcription factor p65²⁸, and other nuclear senescence
137 markers such as p21^{CIP1} and heterochromatin-associated H3K9me3 were strongly increased, or,
138 regarding non-G1-phase-hyperphosphorylated retinoblastoma (Rb) protein, markedly
139 decreased in VIS (Fig. 1f). Hence, viral infection evokes a host cell response reminiscent of

140 and genetically dependent on key features of other well-established types of cellular senescence
141 and their associated secretome.

142 Notably, VIS became detectable in response to a broad spectrum of viruses, including
143 lentivirus, adeno-associated virus (AAV), vesicular stomatitis virus (VSV) and the low-
144 pathogenic human alpha-coronavirus NL63 (HCoV-NL63) in human lung carcinoma and non-
145 malignant epithelial cells (Fig. 1g, Extended Data Fig. 2a; see human primary bronchial
146 HBEpC and nasal HNEpC epithelial cells, and multiplicity-of-infection [MOI]/SA- β -gal
147 relationships in Extended Data Fig. 2b-d). To more closely mimic SARS-CoV-2 infection, we
148 exposed ACE2-expressing HNEpC to SARS-CoV spike protein-pseudotyped VSV
149 glycoprotein G-deletion mutants (VSV- Δ G*/CoV-S and VSV- Δ G*/CoV-2-S), which all
150 induced senescence in these cells in a spike protein-dependent manner, since ACE2-negative
151 NIH3T3 cells²⁹ failed to senesce (Fig. 1h, Extended Data Fig. 2e). Retrovirus- as well as VSV-
152 induced senescence exhibited enhanced reactive oxygen species (ROS) and γ -H2AX DNA
153 damage foci (Extended Data Fig. 2f). Conversely, the ROS scavenger N-acetylcysteine (NAC)
154 reduced γ -H2AX foci and abrogated VIS. Similarly affecting γ -H2AX foci, GS-441524, the
155 active metabolite of the viral RNA polymerase inhibitor Remdesivir, blunted cGAS/STING
156 activation in VSV-infected cells (Extended Data Fig. 2g, h).

157 Importantly, HNEpC infected with the authentic SARS-CoV-2 virus also displayed SASP-
158 positive senescence that was preventable by *shp53*-mediated inability to senesce or by GS-
159 441524 treatment (Fig. 1i, j, Extended Data Fig. 2i, j). Moreover, RNA-seq analysis of SARS-
160 CoV-2-infected alveolar epithelial cells (AEC) as well as publicly available RNA-seq datasets
161 of normal human bronchus epithelial (NHBE) cells and lung cancer cell lines⁴ corroborated
162 robust signs of senescence induction (Fig. 1k, Extended Data Fig. 2k). Thus, virus infection in
163 general and SARS-CoV-2 infection of respiratory epithelial cells in particular evoke full-

164 featured cellular senescence, underscoring our hypothesis that VIS might play a critical
165 pathogenic role in COVID-19 lung disease.

166

167 **Cellular senescence in COVID-19 patients**

168 Next, we asked whether VIS would be a typical feature detectable in SARS-CoV-2-infected
169 patients and specifically analyzed nasopharyngeal and lung tissue specimens from patients with
170 a fatal course of PCR-proven COVID-19. Strikingly, immunohistochemical analyses (IHA) of
171 the senescence markers lipofuscin, p16^{INK4a}, p21^{CIP1}, H3K9me3 and IL-8 as a SASP
172 representative unveiled robust reactivity in samples from infected individuals with or without
173 remaining SARS-CoV-2 RNA *in situ* but not in non-COVID-19 controls (Fig. 2a, Extended
174 Data Fig. 3a). Single-cell (sc)RNA-seq analyses of upper airway mucosa samples provided
175 further evidence of a senescence switch in COVID-19 patients³⁰, showing induced transcript
176 levels of p16^{INK4a} (CDKN2A) and multiple SASP factors not only in SARS-CoV-2-permissive
177 ciliated respiratory epithelial cells but also in macrophages, implying paracrine senescence
178 spreading to SASP-attracted macrophages as well as to other less virus-susceptible p16^{INK4a}-
179 elevated mucosal epithelial cell types in the nasopharyngeal specimens (Fig. 2b). By gene
180 expression profiling (GEP) of upper and lower airway specimens, we found SASP-reminiscent
181 cytokines in COVID-19 specimens induced at the transcript level (Fig. 2c). scRNA-seq data
182 further underscored that predominantly ciliated epithelial cells and macrophages scored
183 positive for p16^{INK4a}/CDKN2A transcripts (Extended Data Fig. 3b).

184 Key components of severe COVID-19 are a cytokine storm and macrophage activation
185 syndrome³. We reasoned that the SASP of senescent upper airway epithelial cells may attract
186 and activate macrophages through paracrine senescence induction³¹, thereby contributing to

187 MAS escalation, a condition in which macrophages subsequently infiltrate the lungs. Notably,
188 COVID-19 lungs showed infiltration by pro-inflammatory CD86⁺ macrophages and an M1-
189 macrophage polarization profile^{32,33} (Fig. 2d, Extended Data Fig. 3c). In serum samples of
190 COVID-19 patients, we found SASP peptides such as IL-8, PAI-1/Serpin E1, CCL2/MCP-1,
191 MMP1, MMP9, and TIMP-1 among the most strongly upregulated factors (Fig. 2e). Selective
192 scanning for clotting-relevant factors by ultra-high-throughput mass spectrometry-based
193 proteomics³⁴ also unveiled a massive induction of those factors in COVID-19 serum probes
194 (Fig. 2f), in line with the transcriptional skewing of GO terms “coagulation” and “complement”
195 in SARS-CoV-2-infected NHBE cells, retrovirally senescent and even OIS or irradiation-
196 senescent HDF cells (Extended Data Fig. 1b, 2k)⁷. Further underscoring the pro-thrombogenic
197 propensity in COVID-19 patients, we detected elevated CD62⁺-marked platelet activation in
198 their blood samples (Extended Data Fig. 3d). Accordingly, clinically more severe cases of
199 COVID-19 exhibited a tight association of higher SASP serum levels, clotting-relevant factors
200 and activated coagulation³⁵ (Fig. 2g, Extended Data Fig. 3e, f), and a close correlation between
201 senescence marker transcripts and microthrombosis in COVID-19 lungs *in situ* (Extended Data
202 Fig. 3g, h). Thus, findings in COVID-19 patient material unveiled alterations consistent with
203 VIS and its SASP in the upper airway epithelia, and suggest SASP-mediated effects as critical
204 contributors to the respective lung disease and associated pro-inflammatory, tissue-damaging
205 and pro-thrombogenic features.

206

207 **Linking COVID-19 features to VIS**

208 Next, we mechanistically interrogated whether supernatant (SN) from VIS cells (SN_{VIS}) might
209 evoke COVID-19-typical functionalities in critical target cell types. Indeed, human THP-1
210 macrophages turned to a CD86⁺ or CD13⁺ M1-like state³² when incubated with SN_{VIS}, but not

211 SN of non-infected proliferating cells (SN_{prol.}) or genetically senescence-incapable virus-
212 infected HDF (Fig. 3a, Extended Data Fig. 4a). They themselves exhibited a strong SASP-
213 reminiscent secretory profile, indicative of paracrine senescence, since only replication-
214 incompetent viruses were used here (Fig. 3b, Extended Data Fig. 4b). Notably, transcripts
215 reminiscent of SN_{VIS}-induced CD86⁺-associated THP1 were similarly detected in COVID-19
216 lungs (Fig. 3c). Indeed, SN_{VIS} exposure enforced paracrine, SA- β -gal-positive senescence in
217 macrophages (Fig. 3d), all in line with their contribution as a VIS-triggered SASP-amplifying
218 cellular messenger to COVID-19 disease. Underscoring the critical role of an altered
219 endothelium as a cytokine-releasing relay³⁶, SN_{VIS} also evoked paracrine senescence in
220 HUVEC human endothelial cells, which, in turn, launched a pro-inflammatory and pro-
221 thrombogenic SASP (Fig. 3e, Extended Data Fig. 4c). Consistent with microangiopathic
222 thrombosis observed in severely affected COVID-19 lungs, transfer of SN_{VIS}, but not SN_{prol.} or
223 SN of virus-infected senescence-incapable HDF, prompted platelet activation³⁷ (Fig. 3f),
224 accelerated clotting time (Fig. 3g), and provoked NET formation *in vitro*⁹ (Fig. 3h). Moreover,
225 mirroring the strongly elevated complement-activating factors in COVID-19 patient samples,
226 we observed enhanced formation of the C5b-C9 membrane attack complex and its ultimate
227 cytotoxic action on HUVEC cells in response to SN_{VIS}-activated human serum (Fig. 3i, j). In
228 essence, the pathogenesis of COVID-19 lung disease appears to be closely linked to
229 senescence-governed immune escalation and pro-thrombotic effects.

230

231 **Eliminating VIS cells by senolytic drugs**

232 Based on these findings we considered VIS cells a central therapeutic target in SARS-CoV-2
233 infection whose early elimination might mitigate the course of disease. Previously, we and
234 others presented evidence that senolysis, *i.e.* the selective depletion of senescent cells by drugs

235 such as Bafilomycin, the BCL-2 family inhibitor ABT-263 (a.k.a. Navitoclax) or the multiple
236 kinases-inhibiting flavonoids Fisetin and Quercetin, the latter typically in combination with the
237 tyrosine kinase inhibitor Dasatinib (D/Q), reduced undesirable local and system-wide effects
238 that persistent senescent cells might otherwise exert³⁸⁻⁴². We first profiled transcript and protein
239 expression of anti-apoptotic BCL-2 family members in VIS cells, and found BCL-xL
240 (BCL2L1), BCL-w (BCL2L2), and MCL-1 (BCL2L3) induced (Fig. 4a, Extended Data Fig. 5a;
241 see also Fig. 2a, Extended Data Fig. 3a, b for elevated BCL2L1 and BCL2L2 expression in
242 COVID-19 patients), thereby providing a rationale for Navitoclax to selectively kill VIS cells.
243 We also found the PI3K/AKT/p70S6K axis, p38MAPK and the tyrosine kinase SRC to be
244 deregulated in VIS, and, hence, to serve as potential targets especially for Fisetin and D/Q
245 according to predicted protein-chemical interactions⁴³⁻⁴⁵ (Fig. 4a, Extended Data Fig. 5b).
246 Indeed, Navitoclax, unlike the BCL-2-specific Venetoclax (a.k.a. ABT-199), as well as Fisetin
247 and D/Q exerted cytotoxic potential selectively against retrovirus- or VSV-driven VIS cells but
248 not equally infected senescence-incapable HDF *in vitro* (Fig. 4b, Extended Data Fig. 5c-e).
249 Considering release of infectious virions as a potential concern, we found no enhanced
250 infectivity upon lysis of VIS cells (Extended Data Fig. 5f, g).

251 Importantly, infection by the authentic SARS-CoV-2 virus rendered HNEpC susceptible to
252 Navitoclax, Fisetin or D/Q (Fig. 4c). Moreover, as seen before with other viruses, SN transfer
253 from SARS-CoV-2-infected cells expanded CD86⁺ THP-1 macrophages, and led to paracrine
254 senescence or complement-mediated lysis of HUVEC cells, if not carried out in *shp53*- or GS-
255 441524-pretreated epithelial cells or under exposure to any of the three senolytic treatment
256 options (Fig. 4d-f, Extended Data Fig. 5h, and i-l regarding VIS, SASP and senolytic
257 susceptibility in the context of the spike protein-affecting SARS-CoV-2 mutations alpha and
258 beta).

259

260 **Senolytic targeting of COVID-19 *in vivo***

261 To determine the impact of senolytic treatment on clinical severity of COVID-19-like lung
262 disease, we first tested early intervention with Navitoclax in the well-established Syrian golden
263 hamster model of SARS-CoV-2-driven lung disease^{46,47}. After intranasal infection with SARS-
264 CoV-2 virus, animals developed COVID19-like pneumonia within the first three to five days.
265 scRNA-seq profiling of SARS-CoV-2-infected vs. mock-infected hamster lungs unveiled
266 upregulated p16^{INK4a}/CDKN2A, core senescence and SASP factor as well as SRC transcript
267 expression in alveolar epithelial cells, macrophages and neutrophils due to primary virus
268 infection or paracrine senescence induction during days 3 to 5 p.i. (Extended Data Fig. 6a). This
269 analysis also demonstrated induction of *BCL-w* transcripts in these cell types at day 5 p.i.
270 (Extended Data Fig. 6b), in support of Navitoclax as a suitable senolytic. Animals on the
271 Navitoclax protocol exhibited moderate adverse effects (Extended Data Fig. 6c, d), presented
272 with profoundly reduced senescent cells and improvement of some histopathological features
273 when compared to a solvent-only-treated but equally SARS-CoV-2-infected cohort on day 7
274 p.i. (Fig. 5a, Extended Data Fig. 6e-g, Extended Data Table 1). Strikingly, we detected much
275 lower concentrations of key pro-inflammatory SASP factors in the serum of Navitoclax-
276 exposed hamsters on day 7 p.i., virtually indistinguishable from uninfected controls (Extended
277 Data Fig. 6h).

278 To evaluate the potential of senolytic intervention in model systems with a more severe
279 COVID-19-like clinical course, we next considered the Roborovski dwarf hamster model⁴⁸. On
280 day 4 p.i. and treatment with either Navitoclax, D/Q or solvent-only, animals with senolytic
281 intervention presented with a substantial reduction of H3K9me3- or lipofuscin-marked
282 senescent cells in their respiratory epithelium, and a profound reduction in lung disease features,

283 especially in the D/Q arm (Fig. 5b-d). Both senolytic regimens also produced in this model a
284 dramatic reduction in SASP-reminiscent serum cytokines on day 4 p.i., close to healthy controls
285 (Fig. 5e). Effects in the D/Q-treated group were particularly meaningful; 5/5 animals survived,
286 displayed no apparent signs of disease and no or only moderate weight loss (Extended Data
287 Fig. 7a). By contrast, 4/5 animals in the Navitoclax- and 3/5 animals in the placebo-treated
288 group had to be terminated due to weight loss and clinical impairment by day 4 p.i. Lastly, we
289 investigated the *K18-hACE2*-transgenic mouse model, which also supports a more severe and
290 typically lethal SARS-CoV-2 infection^{49,50}. Mice were treated comparably to the dwarf hamster
291 model with oral administrations of Navitoclax, D/Q and here also Fisetin, and scheduled for
292 lung analysis on day 6 p.i.. While 2/5 solvent-only-treated and 1/5 Navitoclax-treated mice died
293 on or before day 6, and another Navitoclax-treated mouse just slipped underneath the
294 acceptable weight limit on day 6, all D/Q- and Fisetin-treated mice were alive, had limited
295 weight loss and presented clinically well on day 6 (Extended Data Fig. 7a, b). Although overall
296 histopathological analyses could not unveil overt differences regarding COVID-19-like
297 parameters (Extended Data Fig. 7c, and d regarding virus loads in this and the hamster models),
298 markers of senescent cells were found to significantly lesser extents in the lungs of senolytics-
299 treated mice across all regimens applied (Extended Data Fig. 7e). Moreover, Quercetin was
300 recently tested as an oral formulation with sunflower lecithin against standard care (SC) in two
301 randomized clinical trials (NCT04578158 and NCT04861298) for patients with confirmed
302 SARS-CoV-2 infection and mild COVID-19-associated symptoms. Both trials, based on 152
303 and 42 patients, respectively, demonstrated clinical improvement by the senolytic
304 intervention^{51,52}. Agglomerative hierarchical clustering of the second trial across numerous
305 parameters separated the baseline-indistinguishable patient population by Quercetin vs. SC at
306 day 7 (Fig. 5f, Extended Data Table 2). Moreover, collective analysis of all 194 patients
307 concluded significant risk reductions regarding the needs of hospitalization and oxygen therapy

308 for the Quercetin group, which was also superior to SC in terms of length of hospitalization,
309 referral to the intensive care unit and number of deaths (Extended Data Fig. 8a, b). Taken together,
310 early senolytic intervention during SARS-CoV-2 infection significantly attenuates COVID-19-
311 like lung disease and systemic inflammation.

312 Our investigation marks VIS as a central pathogenic principle and valid therapeutic target in
313 SARS-CoV-2 infection to prevent severe COVID-19 lung disease. The primary virus/host cell
314 encounter evokes a senescence response associated with massive pro-inflammatory cytokine
315 secretion that complements virus spreading to the lower airway tract. Our data pinpoint
316 macrophages as pivotal cellular messengers in this process. Attracted to and primed by upper
317 airway VIS cells, macrophages undergo a secondary, SASP-amplifying senescent state switch.
318 Subsequently deployed in the lungs, they further induce senescence, particularly in endothelial
319 cells. System-wide and locally active pro-coagulatory and complement-activating SASP factors
320 contribute to hallmark histopathological features and clinical severity of COVID-19. Hence,
321 early senolytic intervention is an appealing strategy to interrupt such escalating immune
322 cascade at its beginnings. The D/Q-, Fisetin-, and Navitoclax-mediated effects we observed
323 here are encouraging, but optimized dose-scheduling to maximize their clinical potential and
324 limit potential toxicities is needed. Due to their excellent safety profiles, compounds such as
325 the flavonoids Quercetin and Fisetin are particularly attractive candidates as VIS-targeting
326 senolytics. As already demonstrated for Quercetin^{51,52}, Fisetin is currently being investigated in
327 COVID-19 trials. Robbins and colleagues recently reported enhanced SASP production of pre-
328 existing senescent cells in old mice by pathogen-associated molecular pattern factors such as
329 lipopolysaccharide or the SARS-CoV-2 spike protein⁵³. In turn, pharmacological removal of
330 senescent cells by Fisetin or D/Q in mouse β -coronavirus-infected animals was clinically
331 effective – thereby adding to the rationale of senolytic VIS cell elimination as proposed here

332 for SARS-CoV-2-evoked senescence. Moreover, it will be interesting to explore whether early
333 senolytic intervention may also mitigate chronic post-COVID-19 impairment known as long
334 COVID⁵⁴. Finally, we highlight that although effective vaccinations are available worldwide
335 and will hopefully make COVID-19 history soon, our approach remains conceptually valid in
336 the context of other viral epidemics or pandemics in the future.

337

338 **Online Content** Methods, along with any additional Extended Data display items and Source
339 Data are available in the online version of the paper; references unique to these sections appear
340 only in the online paper.

341

342 **Supplementary Information** is linked to the online version of the paper at
343 www.nature.com/nature.

344

345 **Acknowledgments** We thank Shuetsu Fukushi and Masayuki Saijo (National Institute of
346 Infectious Disease, Tokyo, Japan), Christoph Ratswohl and Kathrin de la Rosa (Max-Delbrück-
347 Center for Molecular Medicine), Vassilis G. Gorgoulis (University of Athens, Greece), Karen
348 Hoffman (Charité – Universitätsmedizin Berlin), and Wolfram Brune (Heinrich Pette Institute,
349 Hamburg, Germany) for materials, Felix Walper (Charité – Universitätsmedizin Berlin) for the
350 support in the BSL3 facility, Florian Kurth, Pinkus Tauber-Lau, Vadim Demichev and Leif
351 Erik Sander on behalf of the Charité PA-COVID-19 study group as well as members of the
352 Charité Core facility high throughput proteomics for data and measurements, Sonia Jangra,
353 Raveen Rathnasinghe, and Randy Albrecht (ISMMS) for support with the BSL3 facility and

354 procedures, Richard Cadagan (ISMMS) for technical assistance; Marion Almeder for handling
355 patient samples; Martino Recchia for the statistical analysis of the data from clinical trials and
356 members of the collaborating labs for discussions and editorial advice. This work was supported
357 by grants to C.A.S. from the Medical Faculty of the Johannes Kepler University, Linz, Austria,
358 the Deutsche Krebshilfe (No. 7011377629), the Deutsche Forschungsgemeinschaft DFG
359 (GO 2688/1-1 | SCHM 1633/11-1, SCHM 1633/9-1), and the Förderverein Hämatologie und
360 internistische Onkologie (Tyle Private Foundation, Linz, Austria), and to S.L. and C.A.S. by
361 the German BMBF e:Med program project SeneSys (No. 031L0189A). Ja.Tr. and A.D.G. were
362 funded by German Research Council Grant SFB-TR84 Z01b. This interdisciplinary work was
363 further made possible by the Berlin School of Integrative Oncology (BSIO) graduate program
364 funded within the German Excellence Initiative (with D.B. as a member of this program), and
365 the German Cancer Consortium (GCC). This research was also partly funded by CRIP (Center
366 for Research on Influenza Pathogenesis), a NIAID funded Center of Excellence for Influenza
367 Research and Surveillance (CEIRS, contract #HHSN272201400008C), and CRIPT (Center for
368 Research on Influenza Pathogenesis and Transmission), a NIAID-funded Center of Excellence
369 for Influenza Research and Response (CEIRR, contract #75N93021C00014), by DARPA grant
370 HR0011-19-2-0020, by supplements to NIAID grant U19AI142733, U19AI135972 and DoD
371 grant W81XWH-20-1-0270, by a Fast Grant of the Mercatus Center and by the generous
372 support of the JPB Foundation, the Open Philanthropy Project (research grant 2020-215611
373 (5384)), and anonymous donors to A.G.-S. and Ma.Ra. is partly funded by the Francis Crick
374 Institute, which receives its core funding from Cancer Research UK (FC001134), the UK
375 Medical Research Council (FC001134), and the Wellcome Trust (FC001134).

376

377 **Author Contributions** S.L., Y.Y., F.B., Ma.Ma., D.B. Sa.Ka., A.L., M.S., Ma.Re. and
378 D.N.Y.F. outlined and performed molecular genetic, biochemical and cell biological
379 experiments in cell lines, primary human and hamster material. Ja.Tr., J.M.A. and N.O.
380 conceptualized and conducted hamster experiments. P.R.-P. carried out bioinformatical
381 analyses. E.W., M.L. and R.E. conceptualized and generated scRNA-seq data. M.P., Se.Ku.,
382 B.P., R.M. and R.L. analyzed tissue specimens from COVID-19 patients and healthy controls.
383 L.K., Ma.Ma. and Jo.To. conceptualized and conducted clotting-related experiments. T.C.F.,
384 K.D., E.G.M. and A.D.G. analyzed the histopathology of hamster and mouse tissues. M.S.,
385 C.M.-R., G.S., M.U. and A.G.-S. conceptualized and conducted mouse experiments. D.N. and
386 C.D. enabled SARS-CoV-2 infections of human cells and contributed to experimental design.
387 R.G., H.J.F.S. and B.L. provided clinical insights and blood samples from COVID-19 patients.
388 C.P. and A.H. processed blood samples and carried out SARS-CoV-2 PCR testing. Mi.Mü. and
389 Ma.Ra. conducted proteome data analysis and interpretation. Su.Ki. and W.H. contributed
390 conceptual input and logistic support regarding specimen collection and virus-based
391 experiments. A.K. and F.D.P. designed and conducted clinical trials on Quercetin in COVID-
392 19 patients. H.S. provided neutralizing antibodies targeting the spike protein of SARS-CoV-2
393 virus and gave experimental recommendations in this regard. S.L. and C.A.S. designed the
394 project, supervised the data analysis and wrote the manuscript.

395

396 **Conflicts of interest** M.U. contributed to this article as an employee of Mount Sinai and the
397 views expressed do not necessarily represent the views of Regeneron Pharmaceuticals Inc.
398 F.D.P. is a member of the Scientific Board of Pharmextracta S.p.A., the vendor of Quevir[®], a
399 dietary supplement containing Quercetin in a sunflower lecithin formulation. The A.G.-S.
400 laboratory has received research support from Pfizer, Senhwa Biosciences, Kenall

401 Manufacturing, Avimex, Johnson & Johnson, Dynavax, 7Hills Pharma, Pharmamar,
402 ImmunityBio, Accurius, Nanocomposix and Merck. A.G.-S. has consulting agreements for the
403 following companies involving cash and/or stock: Vivaldi Biosciences, Contrafect, 7Hills
404 Pharma, Avimex, Vaxalto, Pagoda, Accurius, Esperovax, Farmak and Pfizer. A.G.-S. is
405 inventor on patents and patent applications on the use of antivirals and vaccines for the
406 treatment and prevention of virus infections, owned by the Icahn School of Medicine at Mount
407 Sinai, New York.

408

409 **Author Information** Reprints and permissions information is available at
410 www.nature.com/reprints. The authors declare no competing financial interests.
411 Correspondence and requests for materials should be addressed to C.A.S.
412 (clemens.schmitt@charite.de; clemens.schmitt@kepleruniklinikum.at).

413

414 REFERENCES

- 415 1 Zhang, X. *et al.* Viral and host factors related to the clinical outcome of COVID-19. *Nature*
416 **583**, 437-440, doi:10.1038/s41586-020-2355-0 (2020).
- 417 2 Mehta, P. *et al.* COVID-19: consider cytokine storm syndromes and immunosuppression.
418 *Lancet* **395**, 1033-1034, doi:10.1016/S0140-6736(20)30628-0 (2020).
- 419 3 Merad, M. & Martin, J. C. Pathological inflammation in patients with COVID-19: a key
420 role for monocytes and macrophages. *Nat Rev Immunol* **20**, 355-362, doi:10.1038/s41577-
421 020-0331-4 (2020).
- 422 4 Blanco-Melo, D. *et al.* Imbalanced host response to SARS-CoV-2 drives development of
423 COVID-19. *Cell* **181**, 1036-1045 e1039, doi:10.1016/j.cell.2020.04.026 (2020).
- 424 5 Coppe, J. P., Desprez, P. Y., Krtolica, A. & Campisi, J. The senescence-associated
425 secretory phenotype: the dark side of tumor suppression. *Ann Rev Pathol* **5**, 99-118,
426 doi:10.1146/annurev-pathol-121808-102144 (2010).
- 427 6 Lee, S. & Schmitt, C. A. The dynamic nature of senescence in cancer. *Nat Cell Biol* **21**,
428 94-101, doi:10.1038/s41556-018-0249-2 (2019).

- 429 7 Wiley, C. D. *et al.* SILAC analysis reveals increased secretion of hemostasis-related factors
430 by senescent cells. *Cell Rep* **28**, 3329-3337.e3325, doi:10.1016/j.celrep.2019.08.049
431 (2019).
- 432 8 Ackermann, M. *et al.* Pulmonary vascular endothelialitis, thrombosis, and angiogenesis in
433 Covid-19. *N Engl J Med* **383**, 120-128, doi:10.1056/NEJMoa2015432 (2020).
- 434 9 Middleton, E. A. *et al.* Neutrophil extracellular traps contribute to immunothrombosis in
435 COVID-19 acute respiratory distress syndrome. *Blood* **136**, 1169-1179,
436 doi:10.1182/blood.2020007008 (2020).
- 437 10 Berlin, D. A., Gulick, R. M. & Martinez, F. J. Severe Covid-19. *N Engl J Med* **383**, 2451-
438 2460, doi:10.1056/NEJMcp2009575 (2020).
- 439 11 Wolfel, R. *et al.* Virological assessment of hospitalized patients with COVID-2019. *Nature*
440 **581**, 465-469, doi:10.1038/s41586-020-2196-x (2020).
- 441 12 Hoffmann, M. *et al.* SARS-CoV-2 cell entry depends on ACE2 and TMPRSS2 and is
442 blocked by a clinically proven protease inhibitor. *Cell* **181**, 271-280 e278,
443 doi:10.1016/j.cell.2020.02.052 (2020).
- 444 13 Ju, B. *et al.* Human neutralizing antibodies elicited by SARS-CoV-2 infection. *Nature* **584**,
445 115-119, doi:10.1038/s41586-020-2380-z (2020).
- 446 14 Horby, P. *et al.* Dexamethasone in hospitalized patients with Covid-19 - preliminary report.
447 *N Engl J Med*, doi:10.1056/NEJMoa2021436 (2020).
- 448 15 Xu, X. *et al.* Effective treatment of severe COVID-19 patients with tocilizumab. *Proc Natl*
449 *Acad Sci U S A* **117**, 10970-10975, doi:10.1073/pnas.2005615117 (2020).
- 450 16 Chuprin, A. *et al.* Cell fusion induced by ERVWE1 or measles virus causes cellular
451 senescence. *Genes Dev* **27**, 2356-2366, doi:10.1101/gad.227512.113 (2013).
- 452 17 Martínez, I. *et al.* Induction of DNA double-strand breaks and cellular senescence by
453 human respiratory syncytial virus. *Virulence* **7**, 427-442,
454 doi:10.1080/21505594.2016.1144001 (2016).
- 455 18 Baz-Martinez, M. *et al.* Cell senescence is an antiviral defense mechanism. *Sci Rep* **6**,
456 37007, doi:10.1038/srep37007 (2016).
- 457 19 Hsieh, T. H. *et al.* Senescence in monocytes facilitates Dengue virus infection by increasing
458 infectivity. *Front Cell Infect Microbiol* **10**, 375, doi:10.3389/fcimb.2020.00375 (2020).
- 459 20 Dimri, G. P. *et al.* A biomarker that identifies senescent human cells in culture and in aging
460 skin in vivo. *Proc Natl Acad Sci U S A* **92**, 9363-9367. (1995).
- 461 21 Narita, M. *et al.* Rb-mediated heterochromatin formation and silencing of E2F target genes
462 during cellular senescence. *Cell* **113**, 703-716 (2003).
- 463 22 Yu, Y. *et al.* Targeting the senescence-overriding cooperative activity of structurally
464 unrelated H3K9 demethylases in melanoma. *Cancer Cell* **33**, 322-336 (2018).
- 465 23 Kuilman, T. *et al.* Oncogene-induced senescence relayed by an interleukin-dependent
466 inflammatory network. *Cell* **133**, 1019-1031 (2008).
- 467 24 Jing, H. *et al.* Opposing roles of NF- κ B in anti-cancer treatment outcome unveiled by cross-
468 species investigations. *Genes Dev* **25**, doi:10.1101/gad.17620611 (2011).

- 469 25 Serrano, M., Lin, A. W., McCurrach, M. E., Beach, D. & Lowe, S. W. Oncogenic ras
470 provokes premature cell senescence associated with accumulation of p53 and p16INK4a.
471 *Cell* **88**, 593-602 (1997).
- 472 26 Dou, Z. *et al.* Cytoplasmic chromatin triggers inflammation in senescence and cancer.
473 *Nature*, doi:10.1038/nature24050 (2017).
- 474 27 Liu, S. *et al.* Phosphorylation of innate immune adaptor proteins MAVS, STING, and TRIF
475 induces IRF3 activation. *Science* **347**, aaa2630, doi:10.1126/science.aaa2630 (2015).
- 476 28 Buss, H. *et al.* Constitutive and interleukin-1-inducible phosphorylation of p65 NF- κ B at
477 serine 536 is mediated by multiple protein kinases including I κ B kinase (IKK)-alpha, IKK-
478 beta, IKK-epsilon, TRAF family member-associated (TANK)-binding kinase 1 (TBK1),
479 and an unknown kinase and couples p65 to TATA-binding protein-associated factor II31-
480 mediated interleukin-8 transcription. *J Biol Chem* **279**, 55633-55643,
481 doi:10.1074/jbc.M409825200 (2004).
- 482 29 Wang, P. *et al.* Expression cloning of functional receptor used by SARS coronavirus.
483 *Biochem Biophys Res Commun* **315**, 439-444, doi:10.1016/j.bbrc.2004.01.076 (2004).
- 484 30 Chua, R. L. *et al.* COVID-19 severity correlates with airway epithelium-immune cell
485 interactions identified by single-cell analysis. *Nat Biotechnol* **38**, 970-979,
486 doi:10.1038/s41587-020-0602-4 (2020).
- 487 31 Acosta, J. C. *et al.* A complex secretory program orchestrated by the inflammasome
488 controls paracrine senescence. *Nat Cell Biol* **15**, 978-990, doi:10.1038/ncb2784 (2013).
- 489 32 Roussel, M. *et al.* Mass cytometry deep phenotyping of human mononuclear phagocytes
490 and myeloid-derived suppressor cells from human blood and bone marrow. *J Leukoc Biol*
491 **102**, 437-447, doi:10.1189/jlb.5MA1116-457R (2017).
- 492 33 Li, X. *et al.* The Flavonoid Quercetin Ameliorates Liver Inflammation and Fibrosis by
493 Regulating Hepatic Macrophages Activation and Polarization in Mice. *Front Pharmacol*
494 **9**, 72, doi:10.3389/fphar.2018.00072 (2018).
- 495 34 Messner, C. B. *et al.* Ultra-high-throughput clinical proteomics reveals classifiers of
496 COVID-19 infection. *Cell Syst* **11**, 11-24 e14, doi:10.1016/j.cels.2020.05.012 (2020).
- 497 35 Demichev, V. *et al.* A time-resolved proteomic and prognostic map of COVID-19. *Cell*
498 *Syst*, doi:10.1016/j.cels.2021.05.005 (2021).
- 499 36 Kang, S. *et al.* IL-6 trans-signaling induces plasminogen activator inhibitor-1 from vascular
500 endothelial cells in cytokine release syndrome. *Proc Natl Acad Sci U S A* **117**, 22351-
501 22356, doi:10.1073/pnas.2010229117 (2020).
- 502 37 Beigi, R., Kobatake, E., Aizawa, M. & Dubyak, G. R. Detection of local ATP release from
503 activated platelets using cell surface-attached firefly luciferase. *Am J Physiol* **276**, C267-
504 278, doi:10.1152/ajpcell.1999.276.1.C267 (1999).
- 505 38 Zhu, Y. *et al.* The Achilles' heel of senescent cells: from transcriptome to senolytic drugs.
506 *Aging Cell* **14**, 644-658, doi:10.1111/accel.12344 (2015).
- 507 39 Xu, M. *et al.* Senolytics improve physical function and increase lifespan in old age. *Nature*
508 *medicine* **24**, 1246-1256, doi:10.1038/s41591-018-0092-9 (2018).
- 509 40 Dorr, J. R. *et al.* Synthetic lethal metabolic targeting of cellular senescence in cancer
510 therapy. *Nature* **501**, 421-425, doi:10.1038/nature12437 (2013).

- 511 41 Chang, J. *et al.* Clearance of senescent cells by ABT263 rejuvenates aged hematopoietic
512 stem cells in mice. *Nat Med* **22**, 78-83, doi:10.1038/nm.4010 (2016).
- 513 42 Kirkland, J. L. & Tchkonja, T. Senolytic drugs: from discovery to translation. *J Intern Med*
514 **288**, 518-536, doi:10.1111/joim.13141 (2020).
- 515 43 Freund, A., Patil, C. K. & Campisi, J. p38MAPK is a novel DNA damage response-
516 independent regulator of the senescence-associated secretory phenotype. *EMBO J* **30**,
517 1536-1548, doi:10.1038/emboj.2011.69 (2011).
- 518 44 Bent, E. H., Gilbert, L. A. & Hemann, M. T. A senescence secretory switch mediated by
519 PI3K/AKT/mTOR activation controls chemoprotective endothelial secretory responses.
520 *Genes Dev* **30**, 1811-1821, doi:10.1101/gad.284851.116 (2016).
- 521 45 Jung, S. H. *et al.* Integrin $\alpha\beta4$ -Src-AKT signaling induces cellular senescence by
522 counteracting apoptosis in irradiated tumor cells and tissues. *Cell Death Differ* **26**, 245-
523 259, doi:10.1038/s41418-018-0114-7 (2019).
- 524 46 Kreye, J. *et al.* A therapeutic non-self-reactive SARS-CoV-2 antibody protects from lung
525 pathology in a COVID-19 hamster model. *Cell* **183**, 1058-1069.e1019,
526 doi:10.1016/j.cell.2020.09.049 (2020).
- 527 47 Osterrieder, N. *et al.* Age-dependent progression of SARS-CoV-2 infection in Syrian
528 hamsters. *Viruses* **12**, doi:10.3390/v12070779 (2020).
- 529 48 Trimpert, J. *et al.* The Roborovski dwarf hamster is a highly susceptible model for a rapid
530 and fatal course of SARS-CoV-2 infection. *Cell Rep* **33**, 108488,
531 doi:10.1016/j.celrep.2020.108488 (2020).
- 532 49 Winkler, E. S. *et al.* SARS-CoV-2 infection of human ACE2-transgenic mice causes severe
533 lung inflammation and impaired function. *Nat Immunol* **21**, 1327-1335,
534 doi:10.1038/s41590-020-0778-2 (2020).
- 535 50 White, K. M. *et al.* Plitidepsin has potent preclinical efficacy against SARS-CoV-2 by
536 targeting the host protein eEF1A. *Science* **371**, 926-931, doi:10.1126/science.abf4058
537 (2021).
- 538 51 Di Pierro, F. *et al.* Possible therapeutic effects of adjuvant Quercetin supplementation
539 against early-stage COVID-19 infection: A prospective, randomized, controlled, and open-
540 label study. *Int J Gen Med* **14**, 2359-2366, doi:10.2147/ijgm.S318720 (2021).
- 541 52 Di Pierro, F. *et al.* Potential clinical benefits of Quercetin in the early stage of COVID-19:
542 Results of a second, pilot, randomized, controlled and open-label clinical trial. *Int J Gen*
543 *Med* **14**, 2807-2816 (2021).
- 544 53 Camell, C. D. *et al.* Senolytics reduce coronavirus-related mortality in old mice. *Science*
545 **373**, eabe4832, doi:10.1126/science.abe4832 (2021).
- 546 54 Nalbandian, A. *et al.* Post-acute COVID-19 syndrome. *Nat Med* **27**, 601-615,
547 doi:10.1038/s41591-021-01283-z (2021).
- 548
- 549

550 **FIGURE LEGENDS**

551 **Figure 1 | Senescence is a universal host cell response to viral stress.** **a**, SA- β -gal, SAHF
552 formation by DAPI, and p16^{INK4a} staining of IMR90 five days after retroviral infection or mock
553 control. **b**, GSEA probing senescence-associated genes in WI38 HDF in VIS and OIS. Positive
554 Normalized Enrichment Scores (NES) indicate enrichment compared to proliferating
555 counterparts. Presented NES are statistically significant (FDR q -value < 0.05, Supplementary
556 Information for individual values). **c**, Relative expression of core senescence and SASP
557 transcripts in cells as in *a* by qRT-PCR compared to mock control. **d**, Multiplex bead-based
558 protein analysis in the SN of HDF IMR90 (as in *a*), WI38 and Tig3. **e**, SA- β -gal staining of
559 IMR90 cells expressing JMJD2C, *shp53*, or control vector. **f**, Immunoblot analysis of nuclear
560 senescence markers in samples as in *d*. α -Tubulin as a loading control. **g**, Quantification of SA-
561 β -gal positivity in human cell lines (RPE1, A549) infected with AAV, lentivirus, HCoV-NL63,
562 and VSV. **h**, Quantification of SA- β -gal positivity in human cell lines and primary HNEpC
563 infected with VSV- Δ G*-CoV-S, VSV- Δ G*-CoV-2-S, or VSV- Δ G*/empty vector (VSV- Δ G*-
564 emp). NIH3T3 as ACE2-negative, infection-resistant control. **i**, SA- β -gal staining of stably
565 hACE2-engineered primary nasal epithelial cells (HNEpC-hACE2) infected with SARS-CoV-
566 2 and treated as indicated at 48 hours p.i.. **j**, Relative expression of the indicated transcripts by
567 qRT-PCR of cells as in *i*. **k**, GSEA of RNA-seq-based GEP from AEC infected with SARS-
568 CoV-2 vs. uninfected controls ($n = 4$). Preselected senescence-associated terms with FDR q -
569 value ≤ 0.01 are shown (see Supplementary Information for individual values). All scale bars
570 in this figure represent 100 μ m, except 5 μ m for SAHF in *a*. All quantifications in this figure
571 refer to mean \pm s.d. of $n = 3$ independent experiments (except *k*) with individual values as dots
572 in bar plots or representative photomicrographs shown.

573

574 **Figure 2 | COVID-19 patients exhibit features of VIS. a**, Immunohistochemical analysis
575 (IHA) of senescence markers, BCL-w, and *in situ* hybridization of SARS-CoV-2 RNA in the
576 respiratory mucosa of nasopharyngeal specimens from COVID-19 patients ($n = 6$ for p16^{INK4a}
577 and IL-8, otherwise $n = 5$) vs. non-COVID-19 individuals ($n = 2$). Quantification of affected
578 areas as mean percentages of positive cells \pm s.d. or mean percentage of positive area \pm s.d
579 (lipofuscin only). **b**, scRNA-seq-based GEP of upper airway tissue from COVID-19 patients
580 ($n = 19$) and normal controls ($n = 5$). Color-coded average-scaled (z-scores) expression levels
581 of the respective transcripts and cell types. (n)rMa = (non-)residential macrophage. **c**, GEP of
582 SASP-reminiscent cytokines in upper (nasopharynx) and lower airway (lung) tissue samples
583 from COVID-19 vs. non-COVID-19 autopsies ($n = 3$ each) by oligonucleotide-based transcript
584 hybridization. **d**, CD86-IHA of macrophages in lung specimens from COVID-19 ($n = 13$) vs.
585 non-COVID-19 patients ($n = 6$). Mean number of positive non-epithelial cells in $0.1 \text{ mm}^2 \pm$
586 s.d.. $p = 0.0005$. **e**, Multiplex bead-based protein analysis of serum samples from COVID-19
587 patients ($n = 32$) and healthy donors ($n = 8$). **f**, Mass spectrometry-based proteome analysis of
588 serum from COVID-19 patients ($n = 26$) and healthy donors (serum $n = 3$ and plasma $n = 11$).
589 Heatmaps in **e** and **f** present scaled (z-scores) protein intensities. **g**, 3D-plot showing serum
590 levels of D-Dimer (clotting activity), SERPINA3 (coagulation-related SASP factor), and IL6
591 (pro-inflammatory SASP factor) correlated to WHO-graded clinical COVID-19 severity.
592 $n = 133$ patients; size of the sphere is proportional to the population size. All photomicrographs
593 are representative and scale bars mark $50 \mu\text{m}$ in this figure.

594

595 **Figure 3 | The VIS-associated secretome drives key immune-thrombotic components of**
596 **COVID-19. a**, Percentage of CD86⁺ cells in the THP-1 macrophage population exposed to SN
597 from retroviral VIS vs. proliferating (left) or senescence-incapable (right) IMR90 cells. **b**,

598 Multiplex bead-based protein analysis of the SN of THP-1 exposed to SN as in *a* (SN_{prol.} = SN
599 of proliferating cells, SN_{VIS} = SN of VIS cells), SN_{VIS} without THP-1 cells shown on the right.
600 **c**, GEP of M1-macrophage polarization-related transcripts by RNA-seq of THP-1 cells exposed
601 to SN_{prol.} or SN_{VIS} and sorted for CD86-positivity ($n = 2$ each, left) and by oligonucleotide-
602 based transcript hybridization of lung tissue from COVID-19 vs. non-COVID-19 autopsies
603 ($n = 3$ each, right). **d**, SA- β -gal and the CD86⁺ fraction of THP-1 exposed to SN as indicated.
604 **e**, SA- β -gal and transcript expression by qRT-PCR of HUVEC endothelial cells incubated with
605 the SN as indicated. **f**, Platelet activation measured by ADP release from healthy donor platelets
606 incubated with the SN of IMR90 as in *a*. $n = 5$ donors. **g**, Clotting time in whole blood samples
607 ($n = 4$ healthy donors) mixed with indicated SN volumes (WI38, as in *b*). **h**, NET formation
608 after exposing neutrophils to SN from HDF as in *b*. $n = 4$ healthy donors, two measurements
609 each. **i**, Quantification of the cytolytic complement complex C5b-9 on HUVEC incubated with
610 human serum and SN as indicated. **j**, Cytotoxicity assay of HUVEC as in *i*. All quantifications
611 (mean \pm s.d. with individual values as dots) and representative photomicrographs are from $n = 3$
612 independent experiments except otherwise noted. ‘*’ indicates $p < 0.05$ by unpaired-t-test (two-
613 tailed; *a, f, h, i, j*), unpaired-t-test (one-tailed; *d*), paired-t-test (two-tailed; *g*). All scale bars in
614 this figure represent 100 μ m.

615

616 **Figure 4 | VIS cells are sensitive to senolytic targeting.** **a**, Immunoblot of BCL2 family
617 members (left) and kinases (right) in HDF lysates as indicated. α -Tubulin as a loading control.
618 **b**, Relative viability of IMR90 cells as in Fig. 1e, 48 hours after treatment with senolytics as
619 indicated or solvent-only (DMSO). **c**, Viability of HNEpC-hACE2 infected with SARS-CoV-
620 2 or mock, and treated with senolytics as indicated for *c-f*. **d**, Relative change of the CD86⁺
621 fraction in the THP-1 cell population after receiving SN of HNEpC-hACE2 as in *c*. Of note,

622 SN transfer experiments were carried out in the presence of SARS-CoV-2 neutralizing anti-
623 spike antibodies, preventing transmission of infection (as evidenced by negative target cell
624 SARS-CoV-2 PCR, data not shown). **e**, SA- β -gal staining of HUVEC endothelial cells after
625 receiving SN of HNEpC-hACE2 as in *d*. **f**, Quantification of C5b-9 on HUVEC cells exposed
626 to human serum with SN of HNEpC-hACE2 as in *d*. All bar plots in this figure show mean
627 results \pm s.d. of $n = 3$ independent experiments with individual values as dots. All “*” in this
628 figure indicate $p < 0.05$ by unpaired t-test (two-tailed).

629

630 **Figure 5 | Senolytic targeting mitigates disease features of COVID-19 in animal models**

631 **and patients. a**, H3K9me3 IHA in nasopharyngeal (top) and lung (middle) specimens, as well
632 as lipofuscin-based detection (bottom) of senescent cells in the lung of golden hamsters infected
633 with SARS-CoV-2 and treated with Navitoclax or solvent-only ($n = 5$ animals each), or mock-
634 infected and untreated ($n = 3$ animals) at day 7 p.i.. **b**, H3K9me3 IHA and lipofuscin staining
635 in nasopharyngeal sections of Roborovski dwarf hamsters infected with SARS-CoV-2 or mock,
636 at day 4 p.i. after treatment as indicated. **c** Hematoxylin-eosin (H/E)-stained lung tissue of dwarf
637 hamsters as in *b* on day 4 p.i.; uninfected healthy hamsters (mock) for comparison (xiv–xvii).
638 Lung sections for overview (i, v, x) with signs of COVID-19-like pneumonia and hemorrhage:
639 hyperplasia of bronchial epithelium (double-headed arrow), hemorrhage (asterisks) and
640 necrosis (black arrows) of alveolar epithelial cells with neutrophil infiltration (white arrows),
641 and endothelialitis (lined black arrows). “*” indicates $p < 0.05$ by unpaired-t-test (one-tailed).
642 **d**, Quantification of the findings in *c*. **e**, Multiplex bead-based protein analysis of dwarf hamster
643 serum samples on day 4 p.i. (as in *b-d*). $n = 5$ each (*b-d*; $n = 4$ each in *e*) for SARS-CoV-2-
644 infected and treated animals. $n = 2$ for healthy (mock) control. **f**, Constellation plots of COVID-
645 19 patients⁵² before (day 0) and after 7 days of standard care (SC) only, or Quercetin plus SC.

646 Variables (Extended Data Table 2) were simultaneously analyzed by agglomerative
647 hierarchical clustering to visualize similarity (distance) between patients and separation of the
648 cohorts after treatment. $n = 21$ for each group. All quantifications are mean \pm s.d. All
649 photomicrographs in this figure are representative with scale bars indicating 50 μm (except as
650 indicated in *c*).

651

652 METHODS

653 Cell culture and virus production

654 Cell lines were maintained according to the guideline of suppliers. Human diploid fibroblast
655 (HDF) IMR90, WI38, Tig3 were described previously²². Human cell lines RPE1 (hTERT
656 RPE1), A549 and HUVEC were purchased from ATCC. Primary human nasal or bronchial
657 epithelial cells (HNEpC and HBEpC) were purchased from PromoCell. HNEpC cells with
658 exogenous ACE2 expression (HNEpC-hACE2) were generated by lentiviral infection (hACE2
659 lentivirus, BPS Bioscience). THP-1 cells were kindly provided by Anna Walter (Charité).
660 Senescence-incapable cell lines were generated by transduction with lentiviruses encoding
661 JMJD2C or *shp53* as previously described^{22,55}.

662 All viruses used in this work are tagged with GFP, with the exception of HCoV-NL63 and
663 SARS-CoV-2, and infection efficiency was monitored by detecting fluorescence in infected
664 cells. Retrovirus was produced by transfecting Phoenix packaging cells with a murine stem cell
665 virus (MSCV) GFP plasmid⁵⁶. Lentivirus was produced by transfecting 293T cells with
666 psPAX2, pMD2.G (Addgene nr. 12260 and 12259) and pCDH-CMV-MCS-EF1-GFP
667 plasmids²². AAV was obtained from the Charité Viral Core Facility. Caco-2 cell-adapted wild-
668 type HCoV-NL63 virus at a titer of 3×10^6 pfu/ml was provided by the M.L. lab. VSV-GFP
669 was a kind gift from W. Brune (Heinrich Pette Institute, Hamburg, Germany). VSV-ΔG* GFP
670 (Kerafast) and plasmids encoding SARS-CoV spike (pKS SARS St19; kindly provided by S.
671 Fukushi, National Institute of Infectious Disease, Tokyo, Japan), SARS-CoV-2 spike (Wuhan
672 SARS-CoV-2 spike deltaCT28; kindly provided by C. Ratswohl and K. de la Rosa, MDC),
673 SARS-CoV-2 spike variants Alpha and Beta (pCDH-CMV-spike-B117-EF1-puro and pCDH-
674 CMV-spike-B1351-EF1-puro synthesized by GENEWIZ, China) proteins were used to

675 generate mutant pseudotypes. SARS-CoV-2 (hCoV-19/Germany/BY-ChVir-984/2020,
676 sequence reference EPI_ISL_406862) was propagated for *in vitro* applications in Vero E6 cells
677 (ATCC CRL-1586) and genome-sequenced to exclude stocks with mutations from further
678 experiments. Infection was monitored by PCR, detecting viral genomic RNA in the supernatant
679 48 or 72 h p.i., as previously described⁵⁷. Experiments were conducted under appropriate
680 biosafety conditions with enhanced respiratory personal protection equipment in the BSL-3
681 facility at the Institute for Virology, Charité, Berlin. Self-made virus stocks were concentrated
682 10-times using virus concentrations kit (TaKaRa Bio and Abcam). High-titer virus infection to
683 induce VIS reflect MOI of 50 for replication-incompetent retrovirus and lentivirus, 10 for
684 replication-incompetent AAV and VSV-ΔG*, 10 as well for replication-competent HCoV-
685 NL63, 1 for replication-competent VSV, and 0.1 for replication-competent SARS-CoV-2. VIS
686 features were assessed on day 5 (retrovirus, lentivirus), day 3 (HCoV-NL63, VSV-ΔG*, SARS-
687 CoV-2) or day 2 (VSV) p.i.

688

689 **COVID-19 patients, non-COVID-19 patients and healthy donor material**

690 Upper (nasopharyngeal) and lower airway (lung) tissue FFPE samples were derived from
691 deceased SARS-CoV-2-infected COVID-19 patients as well as archive material from patients
692 who passed away without significant clinical signs of a respiratory infection prior to October
693 2019 (*i.e.* non-COVID-19 patients), blood samples of SARS-CoV-2-infected and hospitalized
694 patients in the course of their COVID-19 disease, or blood samples from healthy volunteers
695 were used based on approval by the local ethics commission of the Johannes Kepler University
696 (reference number 1070/2020). All COVID-19 patients were PCR-proven SARS-CoV-2-
697 positive, however, SARS-CoV-2 RNA was detectable in 4/5 COVID-19 cases shown in Fig.

698 2a. All participants gave informed consent. In addition, we conducted re-analyses of additional
699 patient and control materials that were obtained before and published elsewhere^{30,34,51,52}.

700

701 **Flow cytometry, immunoblotting, immunofluorescence, and immunohistochemical**
702 **analysis**

703 Flow cytometry, immunoblotting (IB), immunofluorescence (IF), and immunohistochemical
704 analysis (IHA) were performed as described previously^{24,58}. Surface antigen detection by flow
705 cytometry was carried out with fluorescence-conjugated antibodies against human CD86-PE-
706 Cy7 (BioLegend, #374209, 1:200), CD13-APC-Cy7 (BioLegend, #301709, 1:200), CD62P-PE
707 (BioLegend, #304905, 1:200). Antigen detection by IB was carried out with antibodies against
708 BCL2 (Cell Signaling Technology [CST], #15071, 1:1000), BCLXL (CST, #2764, 1:1000),
709 BCLW (CST, #2724, 1:1000), MCL1 (CST, #39224, 1:1000), phospho-p65-Ser536 (CST,
710 #3033, 1:1000), phospho-IRF3-Ser386 (CST, #37829, 1:1000), phospho-Rb-Ser807/811 (CST,
711 #8516, 1:1000), p21^{CIP1} (Santa Cruz Biotechnology [SCBT], #sc-6246, 1:200), p16^{INK4a}
712 (SCBT, #sc-1661, 1:200), H3K9me3 (Abcam, #ab8898, 1:2000), phospho-Akt (Thr308) (CST,
713 #13038T, 1:2000), phospho-p38 MAPK (Thr180/Tyr182) (CST, #4511T, 1:1000), phospho-
714 p70 S6 Kinase (Thr389) (CST, #9234T, 1:1000), phospho-Src (Tyr416) (CST, #6943T, 1:1000)
715 and α -Tubulin (Sigma, #T5168, 1:2000). Anti-mouse or anti-rabbit horseradish peroxidase-
716 conjugated antibodies were used as secondary antibodies (GE Healthcare, #RPN4301 and
717 #NA931V, respectively). Antigen detection by IF was performed with antibodies against
718 phospho-H2A.X (Cell Signaling, #9718, 1:400), p16^{INK4a} (Abcam, #ab211542, 1:250), C5b-9
719 (SCBT, #sc-58935, 1:250), anti-mouse-Cy3 secondary antibody (Thermo Fisher, #A10521,
720 1:1000), anti-rabbit-594 secondary antibody (Thermo Fisher, #A11012, 1:1000). Antigen
721 detection by IHA was performed using the HiDef Detection HRP Polymer System (Cell

722 Marque, #954D-30) with antibodies against p21^{CIP1} (SCBT, #sc-6246, 1:200), IL-8 (Abcam,
723 #ab18672, 1:200), H3K9me3 (Abcam, #ab8898, 1:2000), BCL2L2 (Abcam, #ab190952,
724 1:1000), CD86 (Antibodies-online, ABIN736701, 1:100).

725 Original scans of the immunoblot information presented in Fig. 1f and 4a, with molecular
726 weight markers and crop area indicated, are shown in Supplementary Information.

727

728 ***In situ* hybridization (ISH)**

729 ISH was performed as previously described⁴⁶ using the ViewRNA™ Tissue Assay Core Kit
730 (Invitrogen, #19931) and the ViewRNA™ Tissue Assay Blue Module (Invitrogen, #19932)
731 according to the manufacturer's instructions. For the detection of SARS-CoV-2, ViewRNA™
732 Type 1 Probe Set COVID19 polyprotein (Invitrogen, #CVX-06, Assay ID VPNKRHH) and
733 ViewRNA™ Type 6 Probe Set Human ACTB (Invitrogen, #VX-06, Assay ID VA6-10506)
734 were used. Following hybridization, sections were counterstained with hematoxylin and
735 mounted with ProLong™ Glass Antifade Mountant (Invitrogen, #P36982). Images were taken
736 using the Olympus Slide Scanner VS200.

737

738 **Quantification of gene transcription**

739 *Quantitative reverse transcriptase PCR (qRT-PCR)*: RNA isolated from cell pellets using
740 Trizol (Invitrogen) was transcribed to cDNA using SuperScript II reverse transcriptase
741 (Invitrogen). Individual gene expression was analyzed by qRT-PCR using Taqman assays from
742 Applied Biosystems. A list of Taqman assays used here is available in Supplementary
743 Information.

744 *RNA sequencing:* Total RNA was isolated using the RNAeasy Mini kit (Qiagen) and sequenced
745 at the BGI Genomics. Single-cell RNA sequencing (scRNA-seq) was conducted as described⁵⁹.
746 Further processing of the raw sequencing data is described in ‘Statistics and data analysis’.

747 *Oligonucleotide hybridization-based transcriptome profiling:* RNA was extracted from FFPE
748 tissue sections with the PureLink™ FFPE RNA Isolation Kit (Thermo Fisher Scientific, Cat.
749 No.: K156002), hybridized with the probe set of the NanoString nCounter® Human Tumor
750 Signaling 360 Panel (Cat. No.: XT-CSPS-H-T360-12), and analyzed on the NanoString
751 nCounter® SPRINT.

752

753 **Quantification of protein expression**

754 *Multiplex bead-based protein detection (MAGPIX):* MAGPIX assays were conducted
755 according to the manufacturer’s manual with following bead panels: Custom Procartaplex 19-
756 plex (Thermo Fisher Scientific, PPX-19, Assay ID MXAACDR), Custom Procartaplex 4-plex
757 (Thermo Fisher Scientific, PPX-04, Assay ID MXCE4XN), Bio-Plex Pro™ Rat Cytokine 23-
758 Plex Assay (Bio-Rad, 12005641). The assay was measured with the BioPlex® Magpix™
759 Multiplex Reader (Bio-Rad) and analyzed with a 5PL algorithm provided by the Bio-Plex
760 Manager™ software (Version 6.1). Detailed procedures for sample preparation and
761 measurement are described in Supplementary Information. Of note, due to a different
762 normalization procedure, values cannot be cross-read between different panels, *e.g.* Fig. 1d vs.
763 Fig. 3b.

764 *Mass spectrometry-based proteome:* Detailed protocol of sample preparation, mass
765 spectrometry and data processing were previously described³⁴, for further details see also
766 Supplementary Information. Briefly, serum samples were reduced, alkylated, digested and

767 conditioned on a Biomek i7 workstation, and approximately 5 µg of peptides per injection were
768 used for the gradient LC-MS/MS analysis. The raw data were processed using DIA-NN 1.7.12.

769

770 **VIS assays *in vitro***

771 *Growth curve analysis:* HDF IMR90, WI38 or Tig3 cells were infected with MSCV retrovirus
772 at day 0 and day 3, and SA-β-gal activity were measured at day 5. For growth curve analyses,
773 2×10^4 cells were seeded into 12-well plates and cell numbers were counted at day 3, 6 and 9.

774 *2'3'-cGAMP ELISA assay:* Cell cytoplasmic 2'3'-cGAMP concentration was measured using
775 the Caymanchem ELISA kit. Briefly, cells were lysed in M-PER extraction reagent (Thermo
776 Fisher) and 10 µg protein lysate was used to determine 2'3'-cGAMP content.

777 *Analysis of cell viability and senescence:* Viability and cell numbers were analyzed by trypan
778 blue dye exclusion or Guava Viacount (Millipore). SA-β-gal activity at pH 6.0 (for human cells)
779 or pH 5.5 (for rodent cells) as a senescence marker in fresh or cryo-preserved cells was assessed
780 as described⁶⁰. *In situ* detection of lipofuscin as a senescence marker in FFPE samples was
781 carried out with the SenTraGorTM reagent (Lab Supplies Scientific; kindly provided by Vassilis
782 G. Gorgoulis, University of Athens) according to the manufacturer's instructions.

783 *ROS detection:* 20 µM Dihydroethidium (DHE, MedChemExpress) was directly added to cells
784 and incubated at 37°C for 20 minutes. DHE was then washed away with PBS. Cells were fixed
785 in 4% paraformaldehyde and staining intensity was analyzed with Nikon fluorescent
786 microscope.

787

788 VIS supernatant transfer and secondary, paracrine senescence

789 Conditioned medium was then collected from proliferating and VIS cells after 24 hours of
790 incubation and centrifuged at 5,000 rpm for 5 minutes, and the SN (SN_{prol.} or SN_{VIS},
791 respectively) was transferred to HUVEC or THP-1 cells for further analysis. For the SN transfer
792 from SARS-CoV-2-infected HNEpC, self-made neutralizing antibodies against SARS-CoV-2
793 (provided by the H.S. lab) were mixed in to block secondary infection.

794

795 NET formation assay

796 NET formation was measured by the concentration of NET-DNA bound to myeloperoxidase
797 (MPO). Neutrophils were isolated from whole blood of four healthy donors. NET were
798 quantified as previously described⁶¹. Briefly, 10 µg/ml myeloperoxidase (MPO) antibody
799 (Abcam; #ab25989) was immobilized on the surface of black MaxiSorp-treated plates (Thermo
800 Scientific). The plate was subsequently washed with PBS and blocked with 5% non-fat milk
801 for 2 hours at RT. Neutrophils incubated for 4 hours at 37°C in RPMI medium from
802 proliferating or VIS WI-38 or IMR-90 cells were pipetted onto the MPO-coated plate and
803 incubated for 1h at RT. NET quantification was performed using the MPO-DNA PicoGreen
804 assay according to the manufacturer's instructions (Quant-iT PicoGreen dsDNA Assay Kit,
805 Invitrogen). Sample fluorescence was measured using the GloMax Discover microplate reader
806 (Promega).

807

808 Rotational thromboelastometry

809 To measure clotting time, a rotational thromboelastometry assay was performed on a
810 ROTEM[®] delta (Werfen) device according to manufacturer's instructions. INTEM captures
811 intrinsic, platelet-dependent and EXTEM extrinsic, non-platelet-dependent clotting. Whole
812 blood samples of healthy donors were spiked with the SN of WI38 in proliferation or VIS.
813 Exclusion criteria for the healthy donors were coagulation disorders and clotting-affecting
814 medication. Gender distribution was equal among the donors.

815

816 **Platelet activation and ADP release measurement by VIS supernatant**

817 Platelet activation was measured by flow cytometry as percentage of CD62/P-selectin-positive
818 cells in whole blood. To measure VIS-evoked ADP release, 2×10^6 platelets from healthy
819 donors were resuspended in 200 μ l conditioned medium and incubated at 37 °C for 1 hour.
820 Supernatant was collected by centrifugation at $2,000 \times g$ for 5 minutes, and ADP concentration
821 was measured using the ADP Colorimetric Assay Kit II (BioVision) according to the
822 manufacturer's instruction.

823

824 **Complement-mediated cytotoxicity in HUVEC endothelial cells**

825 500 μ l normal human serum of healthy donors was incubated with proliferating or VIS HDF
826 (Fig. 3i, j) or HNEpC (Fig. 4f, Extended Data Fig. 5h) in 5 ml medium at 37°C for 30 minutes.
827 Heat-inactivated (56°C for 30 minutes) serum was used as a control. Supernatant was collected
828 and incubated with HUVEC endothelial cells at 37°C. 2 hours after incubation, HUVEC cells
829 were fixed in 4% paraformaldehyde, and C5b-9 immunofluorescent staining was carried out.

830 Alternatively, 24 hours after incubation, a cytotoxicity assay was performed using the
831 CyQUANT LDH Cytotoxicity commercial kit (Invitrogen).

832

833 **Senolytic treatment *in vitro* and secondary viral infection**

834 VIS cells were treated with Venetoclax (1 μ M), Navitoclax (1 μ M), Fisetin (20 μ M), D/Q
835 (20 μ M, reflecting 2 μ M Dasatinib + 20 μ M Quercetin) or AT-101 (1 μ M) for 48 hours and
836 cell viability was determined by trypan blue staining using the Countess™ II FL Automated
837 Cell Counter (Thermo Fisher). To generate the SN used for secondary viral infection, wild-type
838 MEF were infected with VSV for 6 hours and treated with 1 μ M Navitoclax for 24 hours. SN
839 was centrifuged and filtered through a 0.22 μ m PVDF filter and added to THP-1 cells. After 24
840 hours, secondary infectivity was measured by counting GFP-positive THP-1 cells.

841

842 **SARS-CoV-2-driven COVID-19 animal models**

843 *In vitro* and *in vivo* work related to hamsters was conducted under appropriate biosafety
844 conditions in the BSL-3 facility at the Institute for Virology, Freie Universität Berlin, Germany.
845 All hamster experimentation was approved by the relevant state authority (Landesamt für
846 Gesundheit und Soziales Berlin, Germany [permit number 0086/20]), and performed in
847 compliance with national and international guidelines for care and humane use of animals.
848 Preparation of SARS-CoV-2 virus stock and intranasal infection of Syrian hamsters
849 (*Mesocricetus auratus*) as a faithful *in vivo*-model for COVID-19 lung disease were previously
850 described⁴⁶. Briefly, a SARS-CoV-2 wild-type isolate (BetaCoV/Munich/BavPat2-ChVir984-
851 ChVir1017/2020) was grown in Vero E6 cells. To ensure genetic integrity, passage 3 stocks

852 were genome-sequenced, results showed conformity with the published sequence (GenBank
853 MT270112.1) and confirmed the presence of the furin cleavage site essential for *in vivo*
854 pathogenesis. Anaesthetized male and female hamsters at 6-10 weeks of age were inoculated
855 with 1×10^5 pfu SARS-CoV-2 in a total volume of 60 μ l cell culture medium. Control animals
856 were mock infected with the same volume of cell culture medium. One day after infection,
857 animals were randomized and half of the animals ($n = 5$) received a daily single 85 mg/kg body
858 weight dose of Navitoclax in solvent (60% Phosal PG, 30% PEG 300, 20% ethanol)
859 intraperitoneally for six consecutive days. The other half of infected animals ($n = 5$) received
860 the same volume of solvent only. The control group ($n = 3$) did neither receive virus nor
861 treatment. On day 7 p.i., one day after the last treatment, all hamsters were euthanized, and
862 tissue and peripheral blood samples were prepared for further analyses.

863 The Roborovski dwarf hamster (*Phodopus roborovskii*), a species highly susceptible to a severe
864 course of SARS-CoV-2 infection, was used under the permit mentioned above. Infections were
865 performed as previously described⁴⁸. Female Roborovski dwarf hamsters at 5-7 weeks of age
866 underwent the procedure described above for Syrian hamsters with the exception that the total
867 volume of the inoculum was reduced to 20 μ l. The same virus stock was used. Animals were
868 randomly distributed into three treatment groups ($n = 5$) and one non-infected, non-treated
869 group ($n = 2$). From 6 h hours p.i. on, animals were treated once daily with oral application of
870 Navitoclax at 85 mg/kg, D/Q at 5/50 mg/kg dissolved in 60% Phosal PG, 30% PEG 300, 20%
871 ethanol and mixed 1:1 with strawberry syrup, the placebo-treatment group received the same
872 solvent/syrup combination without drug. On Day 4 p.i., animals were sacrificed and tissue as
873 well as peripheral blood specimens were collected for downstream analyses.

874 Infection of *K18-hACE2* mice (Jax strain 034860) with SARS-CoV-2 was performed according
875 to the approval by the Institutional Animal Care and Use Committee (IACUC) of Icahn School

876 of Medicine at Mount Sinai (ISMMS) as previously reported⁶². Briefly, 6-week old female mice
877 were infected with 1×10^4 pfu SARS-CoV-2 (USA-WA1/2020, BEI resources NR-52281)
878 grown in Vero E6 cells and validated by genome sequencing, and randomly distributed into
879 three treatment groups ($n = 5$ each) and one solvent control group ($n = 5$). From one day after
880 infection, randomly chosen animals were treated with oral application of Navitoclax at
881 85 mg/kg, D/Q at 5/50 mg/kg, and Fisetin at 100 mg/kg dissolved in 60% Phosal PG, 30%
882 PEG 300, 20% ethanol every other day. On Day 6 p.i. (one day after the last treatment), animals
883 were sacrificed and tissue specimens were collected for histopathological analyses.

884 Hamster and mouse lung tissues were processed for histopathology as described⁴⁷ and analyzed
885 by board-certified veterinary pathologists following suggested standard criteria⁶³. Transmission
886 electron microscopy was performed with trachea tissue from infected and treated Syrian golden
887 hamsters. Fixation and further processing of the samples, as well as image acquisition
888 procedures are described in Supplementary Information.

889

890 **Statistics and data analysis**

891 Based on previous experience^{22,24,41,47,50,53,54,57}, sample sizes typically reflect three to five, in
892 some experiments also much higher numbers of individual primary material as biological
893 replicates. All quantifications from staining reactions were carried out by an independent and
894 blinded second examiner and reflect at least three samples with at least 100 events counted
895 (typically in three different areas) each. For patients and animal models, IHA quantification
896 was carried out in SARS-CoV-2-affected areas. Regarding Fig. 5, Extended Data Fig. 6 and 7,
897 quantification of the indicated features was based on the following numbers of individual
898 photomicrographs from animals as indicated in legend and text: *Fig. 5a* – nasopharynx
899 H3K9me3 ($n = 3$ for mock, $n = 6$ for solvent and Navitoclax), lung H3K9me3 and lipofuscin

900 ($n = 3$ for mock, $n = 5$ for solvent and Navitoclax); *Fig. 5b* – H3K9me3 ($n = 5$ for solvent and
901 Navitoclax, $n = 6$ for D/Q), lipofuscin ($n = 5$ for all three groups); *Extended Data Fig. 7e* –
902 p16^{INK4a} ($n = 5$ for solvent, Navitoclax and D/Q, $n = 4$ for Fisetin), H3K9me3 ($n = 4$ for solvent
903 and Navitoclax, $n = 5$ for Fisetin and D/Q), lipofuscin ($n = 5$ for solvent and Navitoclax, $n = 4$
904 for Fisetin, $n = 7$ for D/Q).

905 Data analysis was performed with GraphPad Prism 9. For statistical comparisons, a *t*-test was
906 applied. Unless otherwise stated, a *p*-value < 0.05 was considered statistically significant. For
907 multiple testing corrections the method by Benjamini & Hochberg (BH) to control for false
908 discovery rate was applied⁶⁴. Bioinformatics Analysis was performed in R, version 4.0.3, and
909 Bioconductor 3.12 using various R packages as described in the Supplementary Information in
910 greater detail. High-performance computation has been performed on the Research/Clinic
911 cluster of the Berlin Institute of Health. For further analyses of COVID-19 patient clinical
912 data^{51,52} as presented in *Fig. 5f* and *Extended Data Fig. 8a, b*, JMP Pro 14 (SAS Institute) was
913 used for agglomerative hierarchical clustering, GraphPad Prism9 was used for Fisher's exact
914 test for *p*-values, and a Haldane-Anscombe correction was applied to calculate relative risks.
915 Lipofuscin (SenTraGor[®]) staining was quantified with the pixel counting function of the ImageJ
916 program (bundled with Java 1.8.0_172, NIH)⁶⁵.

917

918 **Data availability**

919 The WI38 VIS- and OIS-derived raw RNA-seq data (*Fig. 1b* and *Extended Data Fig. 1b*) were
920 deposited at the Gene Expression Omnibus (GEO) repository of the National Center for
921 Biotechnology Information (NCBI) under accession number GSE165532
922 (<https://www.ncbi.nlm.nih.gov/geo/query/acc.cgi?acc=GSE165532>). Gene expression data of

923 human AEC cells infected with SARS-CoV-2 (Fig. 1k) are publicly available from at the NCBI
924 GEO under the accession number GSE148729
925 (<https://www.ncbi.nlm.nih.gov/geo/query/acc.cgi?acc=GSE148729>). Raw sequencing data of
926 NHBE, Calu-3 and A549 cells infected with SARS-CoV-2 (Extended Data Fig. 2k) are publicly
927 available at the NCBI GEO under the accession number
928 GSE147507⁴(<https://www.ncbi.nlm.nih.gov/geo/query/acc.cgi?acc=GSE147507>). Seurat
929 objects comprising scRNA-seq datasets of nasopharyngeal, protected specimen brush, and
930 bronchial lavage samples of 19 COVID-19 patients and five healthy controls³⁰, comprising a
931 total of 36 samples that were analyzed in this study (Fig. 2b), are available at FigShare
932 (<https://doi.org/10.6084/m9.figshare.12436517>; covid_nbt_main.rds, covid_nct_loc.rds). The
933 mass spectrometry-based proteome data of serum from COVID-19 patients and healthy donors
934 in Fig. 2f are described³⁴. Patient proteomics data (Fig. 2g, Extended Data Fig. 3e) are publicly
935 available at <https://www.who.int/teams/blueprint/covid-19>, in which disease severity was
936 defined: g3 = hospitalized, no oxygen therapy; g4 = oxygen by mask or nasal prongs; g5 = non-
937 invasive ventilation or high-flow oxygen; g6 = intubation and mechanical ventilation; g7 =
938 ventilation and additional organ support. scRNA-seq data of hamsters infected with SARS-
939 CoV-2 (Extended Data Fig. 6a, b) are available (GSE162208,
940 <https://www.ncbi.nlm.nih.gov/geo/query/acc.cgi?acc=GSE162208>)⁵⁹. All information related
941 to the two randomized trials on early Quercetin intervention in COVID-19 patients
942 (NCT04578158 and NCT04861298) can be found in the respective publications^{51,52} and in
943 Extended Data Table 2.

944

945

946 **REFERENCES for METHODS and EXTENDED DATA**

947

948

- 949 55 Milanovic, M. *et al.* Senescence-associated reprogramming promotes cancer stemness.
950 *Nature* **553**, 96-100, doi:10.1038/nature25167 (2018).
- 951 56 Schmitt, C. A., Rosenthal, C. T. & Lowe, S. W. Genetic analysis of chemoresistance in
952 primary murine lymphomas. *Nat Med* **6**, 1029-1035 (2000).
- 953 57 Corman, V. M. *et al.* Detection of 2019 novel coronavirus (2019-nCoV) by real-time RT-
954 PCR. *Euro Surveill* **25**, doi:10.2807/1560-7917.Es.2020.25.3.2000045 (2020).
- 955 58 Schmitt, C. A., McCurrach, M. E., de Stanchina, E., Wallace-Brodeur, R. R. & Lowe, S.
956 W. INK4a/ARF mutations accelerate lymphomagenesis and promote chemoresistance by
957 disabling p53. *Genes Dev* **13**, 2670-2677 (1999).
- 958 59 Nouailles, G. *et al.* Longitudinal omics in Syrian hamsters integrated with human data
959 unravel complexity of moderate immune responses to SARS-CoV-2. *bioRxiv*,
960 2020.2012.2018.423524, doi:10.1101/2020.12.18.423524 (2020).
- 961 60 Reimann, M. *et al.* Tumor stroma-derived TGF- β limits Myc-driven lymphomagenesis via
962 Suv39h1-dependent senescence. *Cancer Cell* **17**, 262-272 (2010).
- 963 61 Veras, F. P. *et al.* SARS-CoV-2-triggered neutrophil extracellular traps mediate COVID-
964 19 pathology. *J Exp Med* **217**, doi:10.1084/jem.20201129 (2020).
- 965 62 Rathnasinghe, R. *et al.* Comparison of transgenic and adenovirus hACE2 mouse models
966 for SARS-CoV-2 infection. *Emerg Microbes Infect* **9**, 2433-2445,
967 doi:10.1080/22221751.2020.1838955 (2020).
- 968 63 Gruber, A. D. *et al.* Standardization of reporting criteria for lung pathology in SARS-CoV-
969 2-infected hamsters: What matters? *Am J Respir Cell Mol Biol* **63**, 856-859,
970 doi:10.1165/rcmb.2020-0280LE (2020).
- 971 64 Hochberg, Y. & Benjamini, Y. More powerful procedures for multiple significance testing.
972 *Stat Med* **9**, 811-818 (1990).
- 973 65 Schneider, C. A., Rasband, W. S. & Eliceiri, K. W. NIH Image to ImageJ: 25 years of
974 image analysis. *Nat Methods* **9**, 671-675, doi:10.1038/nmeth.2089 (2012).
- 975 66 Fridman, A. L. & Tainsky, M. A. Critical pathways in cellular senescence and
976 immortalization revealed by gene expression profiling. *Oncogene* **27**, 5975-5987,
977 doi:10.1038/onc.2008.213 (2008).
- 978 67 Hari, P. *et al.* The innate immune sensor Toll-like receptor 2 controls the senescence-
979 associated secretory phenotype. *Sci Adv* **5**, eaaw0254, doi:10.1126/sciadv.aaw0254 (2019).
- 980 68 Schleich, K. *et al.* H3K9me3-mediated epigenetic regulation of senescence in mice predicts
981 outcome of lymphoma patients. *Nat Commun* **11**, 3651, doi: 10.1038/s41467-020-17467-z
982 (2020).

983

984 **EXTENDED DATA FIGURE LEGENDS**

985 **Extended Data Figure 1 | Additional biological properties of retroviral VIS. a**, SA- β -gal
986 staining, SAHF formation by DAPI, and p16^{INK4a} staining of HDFs (Tig3 and WI38) five days
987 after retroviral infection or mock control. Representative photomicrographs of $n = 3$
988 independent experiments. **b**, Gene set enrichment analysis (GSEA) of virus infection-relevant
989 GO terms probing RNA-seq datasets of WI38 HDF in VIS and OIS. Positive normalized
990 enrichment scores (NES) indicate enrichment in VIS (dark grey bars) or OIS (light grey bars)
991 compared to proliferating counterparts (mock infection for VIS, or empty vector control for
992 OIS). NES with FDR q -value ≤ 0.1 are considered statistically significant and presented (for
993 individual q -values, see Supplementary Information); $n = 3$ biological replicates each. **c**, Gene
994 expression analysis for core senescence and SASP genes by quantitative RT-PCR in WI38 and
995 Tig3 as in *a*. Mean relative transcript level compared to mock control + s.d. of $n = 3$ independent
996 experiments are shown. **d**, Growth curve analyses of HDF infected with retrovirus at different
997 MOI as indicated, showing that high-titer virus induced VIS, reflected by stable cell numbers
998 over time, while lower virus titer remained compatible with exponential cell growth. $n = 3$
999 independent experiments are presented as mean cell numbers \pm s.d.. **e**, SA- β -gal staining (left)
1000 and gene expression analysis of the indicated transcripts by qRT-PCR (right) in wild-type (WT)
1001 or senescence-defective $p53^{-/-}$ MEF, five days after infection with high-titer retrovirus or mock
1002 as a control. Representative photomicrographs with fractions of SA- β -gal-positive cells, and
1003 mean relative transcript levels normalized to mock control \pm s.d. of $n = 4$ independent
1004 experiments are shown. **f**, Gene expression analysis of the indicated transcripts by qRT-PCR in
1005 IMR90 cells expressing JMJD2C, *shp53*, or control vector as in Fig. 1e. **g**, Multiplex bead-
1006 based protein analysis of SN of senescence-incapable IMR90 as in Fig. 1e. $SN_{\text{mock}} = SN$ of
1007 mock-infected cells; $SN_{\text{virus}} = SN$ of retrovirus-infected cells. Mean expression levels of $n = 3$
1008 biological replicates are shown. **h**, cGAS/STING activation upon viral infection, as evidenced

1009 by a higher induction of cyclic guanosine monophosphate-adenosine monophosphate (2'3'-
1010 cGAMP) by ELISA analysis in matched pairs of HDF after either mock or retrovirus infection
1011 (mean of $n = 4$ independent experiments for each cell line, upper panel). Mean cGAMP levels
1012 + s.d. for senescence-incapable IMR90 as in Fig. 1e ($n = 4$ independent experiments, lower
1013 panel). **i**, SA- β -gal staining of IMR90 cells, treated with reverse transcriptase inhibitor
1014 azidothymidine Zidovudine (50 μ M), cGAS inhibitor G150 (5 μ M), STING inhibitor H-151
1015 (1 μ M), or DMSO. Mock infection and DMSO solvent treatment as negative controls.
1016 Representative photomicrographs and quantification of positively stained cells as mean \pm s.d.
1017 of $n = 3$ independent experiments are shown. **j**, 2'3'-cGAMP ELISA analysis of VIS IMR90
1018 cells as in *i*.

1019

1020 **Extended Data Figure 2 | Additional biological properties of VIS exerted by a variety of**
1021 **viruses. a**, SA- β -gal staining in human cell lines (RPE1, A549) infected with AAV, lentivirus,
1022 HCoV-NL63, and VSV as in Fig. 1g. **b**, SA- β -gal staining of human primary bronchial or nasal
1023 epithelial cells (HBEpC and HNEpC, respectively) infected with HCoV-NL63 and VSV. Mock
1024 infected cells as negative control. Quantification of positive cells for $n = 3$ independent
1025 experiments is shown as mean \pm s.d.; scale bar = 100 μ m. **c**, Quantification result of SA- β -gal-
1026 positive cells (RPE1, A549) after lentiviral infection at MOI as indicated are shown as mean
1027 percentage \pm s.d. for $n = 3$ independent experiments. Note that MOI 50 was chosen for VIS
1028 induction. **d**, Quantification result of SA- β -gal-positive RPE1 cells after infection with VSV-
1029 Δ G*-CoV-S or VSV- Δ G*-CoV-2-S at MOI as indicated are shown as mean percentage \pm s.d.
1030 for $n = 3$ independent experiments. Note that MOI 10 was chosen for VIS induction. **e**, SA- β -
1031 gal staining in human cell lines (RPE1, A549) and primary HNEpC infected with VSV- Δ G*-
1032 CoV-S, VSV- Δ G*-CoV-2-S, or VSV- Δ G*/empty vector (VSV- Δ G*-emp) as in Fig. 1g.

1033 NIH3T3 as ACE2-negative, infection-resistant control. **f**, Fluorescence detection of ROS in
1034 IMR90 after infection with retrovirus or VSV and treatment with NAC as indicated (upper
1035 panels). SA- β -gal staining and quantification of corresponding samples (lower panels). Mock
1036 infection or solvent treatment controls (UT) are shown. Representative photomicrographs and
1037 quantification are shown as mean percentages \pm s.d. for $n = 3$ independent experiments. Scale
1038 bar for ROS and SA- β -gal = 100 μ m; for γ H2A.X (insets; pink dots reflect foci) 5 μ m. **g**,
1039 Quantification of γ H2A.X-positive IMR90 cells as in *f*. $n = 3$ independent experiments is shown
1040 as mean \pm s.d. **h**, 2'3'-cGAMP ELISA analysis of IMR90 infected and treated with GS-441524
1041 as in *g*. $n = 8$ independent experiments is shown as mean \pm s.d. **i**, Viral RNA detection in the
1042 supernatant of primary nasal epithelial cells with exogenous hACE2 expression (HNEpC-
1043 hACE2) infected with SARS-CoV-2, at the indicated time-points. *shp53* renders cells
1044 senescence-incapable, but, unlike treatment with 10 μ M GS-441524 (GS), does not block viral
1045 replication. Data are shown as mean values + s.d. for $n = 3$ independent experiments. **j**, Relative
1046 viability of the indicated conditions, each compared to the corresponding untreated (UT) control
1047 of SARS-CoV-2-infected or mock-infected cells as in *i*, 72 hours p.i. Data are shown as mean
1048 values + s.d. for $n = 3$ independent experiments. **k**, GSEA probing selected senescence-related
1049 gene sets⁶⁶ by RNA-seq (GSE147507) analysis of NHBE, Calu-3, and A549 cells infected with
1050 SARS-CoV-2, compared to corresponding mock-infected controls. Positive NES indicate
1051 enrichment in virus-infected cells (dark grey bars), negative NES indicate downregulation in
1052 virus-infected cells (light grey bars). NES of FDR q -value < 0.05 are considered statistically
1053 significant and presented (for individual q -values, see Supplementary Information). Biological
1054 replicates comprise $n = 7$ control and $n = 3$ infected regarding NHBE, $n = 3$ for each condition
1055 regarding Calu-3, and $n = 5$ control and $n = 3$ infected regarding A549.

1056

1057 **Extended Data Figure 3 | Vignettes of VIS in human COVID-19 lung specimens. a**, IHA
1058 of senescence markers in autopsy lung specimens from non-COVID-19 individuals (with no
1059 obvious airway pathology) vs. SARS-CoV-2-PCR-proven COVID-19 patients. Representative
1060 photomicrographs and quantification of affected area as mean percentages of positive cells \pm
1061 s.d. or mean percentage of positive area \pm s.d (only for lipofuscin) of COVID-19 patients
1062 (lipofuscin, p21^{CIP1}, H3K9me3, BCL2L2, $n = 5$; IL-8, $n = 9$; SARS-CoV-2 RNA, $n = 4$) and
1063 Non-COVID-19 individuals ($n = 2$). Note that *in situ* hybridization of SARS-CoV-2 RNA was
1064 occasionally, but not consistently positive in COVID-19 samples at autopsy (2/4). Scale bars
1065 represent 50 μ m. **b**, scRNA-sequencing-based expression analysis of *CDKN2A* and targets of
1066 Navitoclax (*BCL2L1* and *BCL2L2*) in bronchiolar protected specimen brushes (PS), and
1067 bronchoalveolar lavages (BL) of COVID-19 patients with critical course of the disease ($n = 4$).
1068 UMAPs of cell types (top). Orange color code marks cells expressing *CDKN2A*, purple *BCL2L1*
1069 (lower left) or *BCL2L2* (lower right), and red for both. **c**, Gene expression profile (GEP)
1070 indicating elevated transcript expression of cytokines and markers related to M1 macrophage
1071 polarization and activation^{32,33} by oligonucleotide-based transcript hybridization of lung
1072 specimens as in *a* ($n = 3$ each). **d**, CD62/P-selectin-marked platelet activation by flow
1073 cytometry in whole blood samples of healthy donors ($n = 7$) or COVID-19 patients ($n = 10$).
1074 Mean \pm s.d. with individual values as dots. $*p = 0.0368$ by unpaired t-test (two-tailed). **e**,
1075 Volcano plot of proteins differentially ($p < 0.05$) expressed in COVID-19 patient serum; SASP
1076 factor SERPINA3⁶⁷ highlighted in red as presented in Fig. 2g. Combined clinical COVID-19
1077 severity WHO grade 3 and grade 4 ($n = 86$ patients) vs. grade 7 ($n = 52$ patients) are compared.
1078 Log2-fold changes are plotted against log10 adjusted (Benjamini-Hochberg) p -values. Vertical
1079 red lines indicate log-fold change cutoffs -0.5/0.5, horizontal red line indicates a significance
1080 cutoff $p = 0.05$. Analysis was performed using the DEqMS software package. **f**, Scatter plot
1081 showing average level of 16 SASP factors measured as in Fig. 2e and fibrinogen concentration

1082 in the serum (y-axis) of the same individual patients. $n = 3$ severe, $n = 5$ moderate, and $n = 18$
1083 mild COVID-19 patients and healthy control ($n = 6$) are shown as color-coded dots. Correlation
1084 coefficient (Pearson) $r = 0.4139$ with $p = 0.0103$. **g**, Expression levels of senescence-related
1085 transcripts (gene sets: Reactome_SASP and SASP_Schleich⁶⁸) by oligonucleotide-based
1086 transcript hybridization of nasopharyngeal and lung specimens of COVID-19 patients ($n = 3$)
1087 separated by their histopathological microthrombosis status. Shown are genes with fold-
1088 change > 1.5 . **h**, Percentages of IL-8-positive cells in COVID-19 lung specimens as in *a*, now
1089 stratified by their microthrombosis status (positive, $n = 4$; negative $n = 5$), are shown as mean
1090 values + s.d.. $p = 0.0397$ by unpaired t-test (two-tailed).

1091

1092 **Extended Data Figure 4 | Additional COVID-19-relevant biological features evoked by**
1093 **the VIS-associated secretome.** **a**, Percentage of CD13⁺ THP-1 macrophages exposed to SN
1094 from retroviral VIS vs. proliferating HDF as indicated and shown in Fig. 3a. $n = 3$ ($n = 4$ for
1095 medium control) independent experiments; shown are mean percentages + s.d.. ‘*’ indicates p
1096 = 0.0017 for IMR90 and 0.0029 for WI38 by unpaired t-test (two-tailed). **b**, GSEA of SN_{VIS}-
1097 primed macrophages unveiled vignettes of senescence and inflammation in the CD86⁺
1098 population by probing of selected senescence- or macrophage activation-related GO terms and
1099 gene sets^{66,68} in RNA-seq analyses of THP-1 macrophages incubated with IMR90 SN_{VIS} and
1100 sorted by CD86 expression status (as in Fig. 3c, left). $n = 2$ for each condition. Gene sets with
1101 FDR q -value ≤ 0.05 are shown. **c**, SA- β -gal staining (left) and gene expression analysis by qRT-
1102 PCR (right) of HUVEC endothelial cells that entered secondary, paracrine senescence upon
1103 exposure to SN_{VIS} of WI38 as indicated. Representative photomicrographs and quantification
1104 of $n = 3$ independent experiments; shown are mean percentages \pm s.d.. Relative expression

1105 levels of core senescence-related transcripts (left panel) and SASP transcripts (right panel) are
1106 shown as mean values + s.d.

1107

1108 **Extended Data Figure 5 | Targets of senolytic drugs are induced after viral infection and**
1109 **render VIS cells sensitive to senolytics. a**, Gene expression analysis of BCL2 family
1110 transcripts by qRT-PCR in VIS HDF, with mock infection as a control, as indicated. $n = 3$
1111 independent experiments for each cell line and infection. **b**, STITCH plot showing interactions
1112 between senolytic drugs (Navitoclax, Fisetin, Dasatinib, Quercetin) and their potential targets.
1113 Protein-protein interactions are shown in grey, chemical-protein interactions in green and
1114 interactions between chemicals in red. Modified from <http://stitch.embl.de>. Note that all
1115 senolytics shown are working in close proximity and have overlapping targets at the level of
1116 kinase networks and BCL2-family members. **c**, Relative viability of proliferating or VIS
1117 (retrovirus) WI38 and Tig3 HDF as in Extended Data Fig. 1a, 24 hours after treatment with
1118 1 μ M Venetoclax, 1 μ M Navitoclax, or solvent-only (DMSO). $n = 3$ independent experiments.
1119 **d**, Relative viability of senescence-incapable IMR90 (as in Fig. 1e and 4b) infected with VSV,
1120 and 24 hours after treatment with 1 μ M Venetoclax, 1 μ M Navitoclax, 20 μ M Fisetin, 20 μ M
1121 D/Q or solvent-only (DMSO). $n = 3$ independent experiments. **e**, Relative viability of
1122 proliferating or VIS IMR90 HDF compared to solvent-only (DMSO) control, two days after
1123 treatments with 1 μ M Navitoclax, 1 μ M MCL1 inhibitor AT101, or both. Results shown as
1124 mean relative viability + s.d. for $n = 3$ independent experiments. Of note, strongly Mcl-1-
1125 expressing IMR90 VIS cells (see Fig. 4a) were not more susceptible to combined treatment
1126 with Navitoclax plus an Mcl-1 inhibitor as compared to Navitoclax alone. **f**, Secondary viral
1127 infectivity by SN transfer. Wild-type MEF that entered VIS in response to replication-
1128 competent VSV/GFP (or mock) were treated with 1 μ M Navitoclax before transferring the SN

1129 to uninfected THP-1 macrophages, here used as an infectivity reporter line. SA- β -gal staining
1130 to illustrate VIS, and GFP detection to visualize VSV infection of MEF. Secondary infectivity
1131 was measured as the GFP-positive fraction of THP-1 cells exposed to SN from MEF after
1132 Navitoclax or solvent-only treatment (bar plot). Senescence-dependent killing of VIS MEF did
1133 not increase GFP-positive THP-1 cells, thereby demonstrating that non-assembled cytoplasmic
1134 virus material potentially released upon senolysis does not add to infectivity. $n = 3$ independent
1135 experiments. **g**, Secondary viral infectivity (% GFP) and relative viability (Rel. viability) of
1136 THP-1 cells after SN transfer from VSV (or mock)-infected MEFs. Dilution of VIS SN as
1137 indicated below decreases secondary infection and increases viability. $n = 3$ independent
1138 experiments. **h**, Viability of HUVEC endothelial cells after exposure to human serum and SN
1139 of proliferating (SN_{prol.}) or VIS (SN_{VIS}) primary nasal epithelial cells (HNEpC-ACE2) as in
1140 Fig. 4f. $n = 3$ independent experiments. **i – l**, SARS-CoV-2 spike protein-pseudotyped VSV-
1141 Δ G*/CoV-2-S system to probe VIS in response to spike protein-affecting mutations. **i**, SA- β -
1142 gal staining of human cell line RPE1 infected with VSV- Δ G*-CoV-2-S (WT), VSV- Δ G*-CoV-
1143 2-S variant B.1.1.7 (Alpha), VSV- Δ G*-CoV-2-S variant B.1.351 (Beta), or mock infection as
1144 control. No obvious difference in the ability to drive VIS was detected. Representative
1145 photomicrographs and quantifications are shown as mean percentages \pm s.d. for $n = 3$
1146 independent experiments. Scale bar represents 100 μ m. **j**, CD86-marked activation of THP-1
1147 cells exposed to SN of RPE1 cells in VIS after infection with VSV- Δ G* pseudotypes as
1148 indicated, or mock infection, as in *i*. Fractions of CD86⁺ cells relative to mock are shown. SN
1149 of cells infected with either mutant- or wild-type-pseudotyped virus equally enhance the
1150 fraction of CD86⁺ THP-1 cells. $n = 3$ independent experiments. **k**, Viability of cells as in *i*, after
1151 senolytic treatments as indicated. $n = 3$ independent experiments. All senolytic regimens,
1152 Navitoclax, Fisetin and D/Q proved equally effective in selectively eliminating VIS cells
1153 induced by the wild-type or the alpha or beta mutants. **l**, Gene expression analysis of

1154 senescence-related genes by qRT-PCR in RPE1 cells as in *i*. While transcript profiles of cell-
1155 autonomous senescence markers and pro-coagulatory SASP factors were similar between wild-
1156 type and mutants, pro-inflammatory cytokines and extracellular matrix-active factors appeared
1157 to be significantly higher expressed in the two mutant scenarios compared to wild-type. $n = 3$
1158 independent experiments. All bar plots in this figure show mean results + s.d. with individual
1159 values as dots. “*” indicates $p < 0.05$ by unpaired t-test (two-tailed) in all panels of this figure.

1160

1161 **Extended Data Figure 6 | Senolysis as a novel treatment concept in the COVID-19 golden**

1162 **hamster model. a**, scRNA-seq-based expression analysis of viral RNA and senescence-
1163 associated genes in SARS-CoV-2-infected Syrian golden hamster lungs ($n = 3$ per time-point).

1164 UMAPs of cell types (top left, cell types of special interest in red), core senescence genes (top
1165 right), *CDKN2A* (bottom left), SASP genes (bottom second from left), and *SRC* (bottom right)

1166 on the indicated day p.i.; orange color code marks cells expressing senescence-associated genes,

1167 purple viral RNA, and red both. **b**, scRNA-seq-based expression analysis of *BCL-w*, *BCL2* and

1168 *MCL1* transcripts in the indicated cell types in SARS-CoV-2-infected Syrian golden hamster

1169 lungs ($n = 3$ per time-point) at the indicated days p.i.; average-scaled (z-scores) expression

1170 levels are shown in color code. Note that *BCL-2* and *MCL-1* transcript levels followed no clear

1171 trend, while *BCL-w* transcripts were induced at day 5 p.i. in all cell types presented. **c**, Daily

1172 body weight assessment of Syrian golden hamsters infected with SARS-CoV-2 (or uninfected

1173 healthy controls), and subsequently treated with Navitoclax or solvent-only as in Fig. 5a. $n = 5$

1174 each for SARS-CoV-2-infected solvent-only- and Navitoclax-treated animals; $n = 3$ for the

1175 healthy control group. **d**, Number of platelets per 500 erythrocytes in blood smears of golden

1176 hamsters infected with SARS-CoV-2 and treated as in *c*, on day 7 p.i.. Mean counts \pm s.d. of

1177 $n = 5$ hamsters per treatment group. * $p = 0.0127$ by unpaired t-test (two-tailed). Note for *c* and

1178 *d*: Although the Navitoclax group presented with relative weight loss of around nine percent
1179 and a reduction of nearly 40% of the initial thrombocyte concentration compared to the
1180 infection-only group at the end of therapy, a prominent adverse effect of Navitoclax, no obvious
1181 external or internal signs of enhanced hemorrhage was observed. *e*, Transmission electron
1182 microscopy analysis of trachea epithelial cells from hamsters as in *b* and *c*. In infected and
1183 solvent treated animals (with the enlarged photomicrograph of a nucleus on the right), ciliated
1184 epithelial cells show senescent features as dilated endoplasmic reticulum (*), disrupted and
1185 dilated nuclear envelope (N = nucleus), vacuolization and altered mitochondria. Scale bar =
1186 1 μ m. *n* = 4 for SARS-CoV-2 infected groups and *n* = 3 for the mock infection group. *f*,
1187 Representative photomicrographs of H/E-stained lung tissue of Syrian golden hamsters as in
1188 Fig. 5a and *c-e* at day 7 p.i.. Lung sections for overview (i, v, ix) with active inflammation
1189 (arrow), signs of necrosis (inset, arrowhead), and hyperplasia (arrowheads) of alveolar
1190 epithelial cells (AEC) II (ii, vi). Vascular endothelialitis (iii, vii) with sloughing of endothelial
1191 cells (arrow), and subendothelial infiltration by lymphocytes (arrowhead). Regeneration of
1192 bronchial epithelium (iv, viii; double-headed arrow). Lung of mock-infected, untreated animals
1193 as control (ix, x, xi, xii). General signs of inflammation and AEC II hyperplasia in the
1194 Navitoclax group were rather similar to untreated animals. while the Navitoclax group
1195 presented with a less extensive patchy pneumonia pattern when compared to the solvent-only
1196 group (compare *f-v* to *f-i*). *n* = 5 each for SARS-CoV-2-infected solvent-only- and Navitoclax-
1197 treated animals. *n* = 3 for the healthy control group. Scale bars in i, v, ix = 1 mm, ii-iv, vi-viii,
1198 x-xii = 50 μ m, insets ii, vi, x = 20 μ m. *g*, Quantification of the findings shown in *f*. **p* = 0.0042
1199 by unpaired t-test (two-tailed). *h*, Multiplex bead-based protein analysis of golden hamster
1200 serum samples at day 7 p.i.; hamsters as in *c-g*. All bar plots in this figure show mean results +
1201 s.d. with individual values as dots.

1202

1203 **Extended Data Figure 7 | Senolysis as a novel treatment concept in COVID-19 in**
1204 **additional animal models. a,** Daily body weight assessment of dwarf hamsters and *K18-*
1205 *hACE2* mice infected with SARS-CoV-2 (or uninfected healthy controls), and subsequently
1206 treated with senolytics as in *b-e* and Fig. 5b-e. Dwarf hamsters: $n = 5$ each for SARS-CoV-2-
1207 infected solvent-only-, Navitoclax- or D/Q-treated; $n = 2$ for the healthy control group. *K18-*
1208 *hACE2*-transgenic mice: $n = 5$ for solvent, Navitoclax, and D/Q; $n = 4$ for Fisetin. **b,** Survival
1209 rate of *K18-hACE2*-transgenic mice on day 6d p.i. with SARS-CoV-2 and subsequent senolytic
1210 treatment as in *a*. **c,** Histological scoring of H/E-stained lung tissue of *K18-hACE2* mice as in
1211 *a, b*. **d,** Viral load in hamster and mouse tissues on day 6 (mouse, as in *a-c*), day 7 (golden
1212 hamster, as in Fig. 5a and Extended data 6), and day 4 (dwarf hamster, as in Fig. 5b-e) p.i.. **e,**
1213 IHA of senescence markers (p16^{INK4a}, H3K9me3) and lipofuscin-staining in lung specimens of
1214 *K18-hACE2*-transgenic mice as in *a-d*. All bar plots in this figure show mean results + s.d. with
1215 individual values as dots.

1216

1217 **Extended Data Figure 8 | Senolysis as a novel treatment concept in COVID-19 patients. a,**
1218 Frequency (bars) and risk (odds ratio) of COVID-19 patients to be hospitalized or in need of
1219 oxygen support after either standard care (SC) or Quercetin plus standard care (Quercetin).
1220 $n = 97$ for each group, based on two randomized trials combined and re-analyzed here^{51,52}. **b,**
1221 Days of hospitalization (left) of COVID-19 patients (left; $*p < 0.0001$ by unpaired t-test, two-
1222 tailed), the fraction of patients admitted to the intensive care unit (ICU; middle) or deceased in
1223 the course of the disease (right). Note that there was no patient in ICU or deceased in the
1224 Quercetin group. Patients as in *n*; $n = 97$ for each group.

1225

1226 **Extended Data Table 1 | Histological scoring of COVID-19 features in the SARS-CoV-2-**
1227 **infected hamsters.** Histopathological scoring of FFPE lung tissue from hamsters infected and
1228 treated as indicated.

1229 * % affected score is scaled as (0) not present, (1) present but $\leq 25\%$, (2) > 25 but $\leq 50\%$, (3)
1230 > 50 but $\leq 75\%$, (4) $> 75\%$;

1231 ** degree of inflammation is scaled as (1) minimal, (2) mild, (3) moderate or (4) severe.

1232 For all other parameters, rating refers to occurrence rate of (1) sporadic, (2) mild, (3) moderate,
1233 (4) severe.

1234 ¹Pneumonia score is the average of five pneumonia criteria (% affected score, degree of
1235 inflammation, occurrence rates of lymphocytes, macrophages, neutrophils).

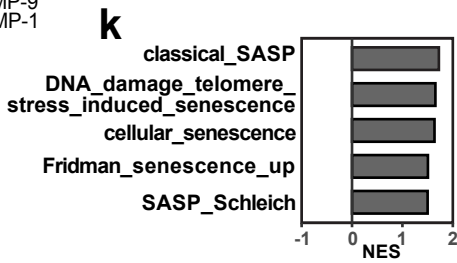
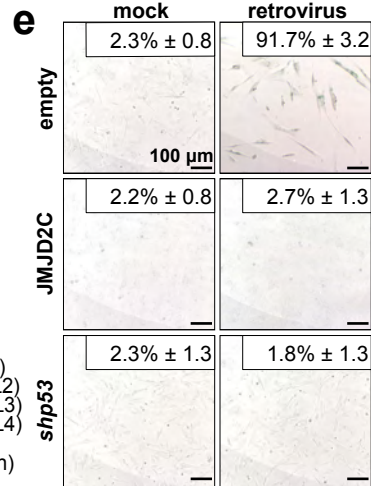
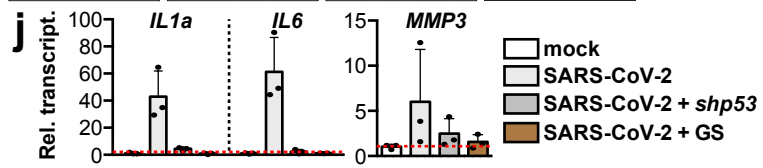
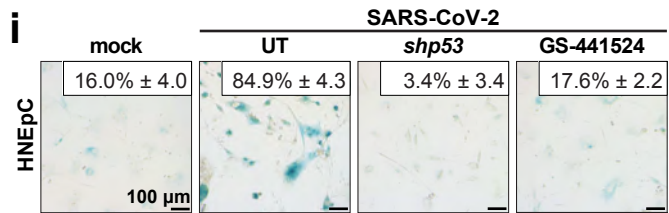
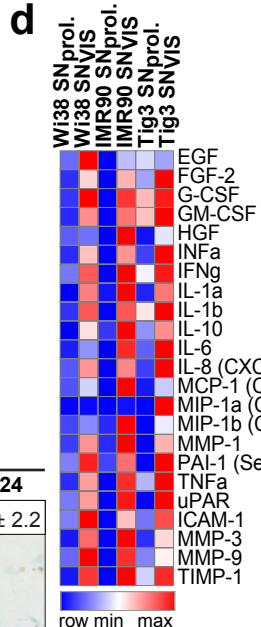
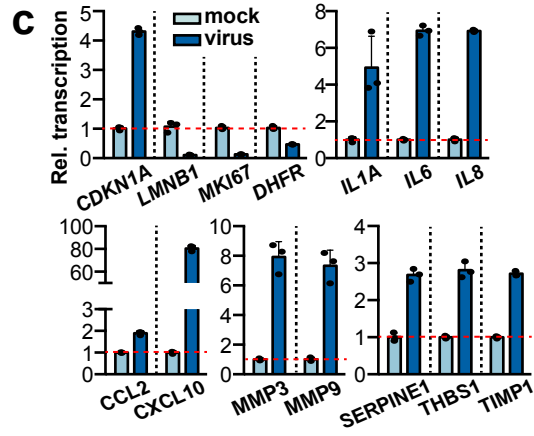
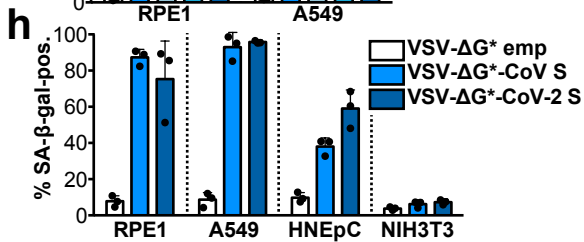
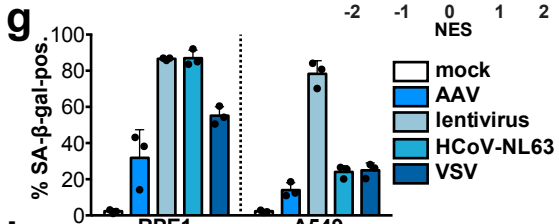
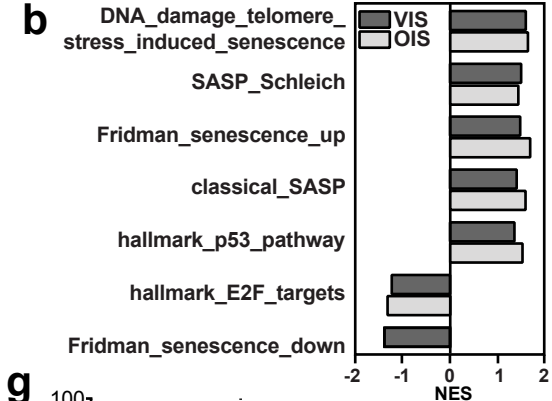
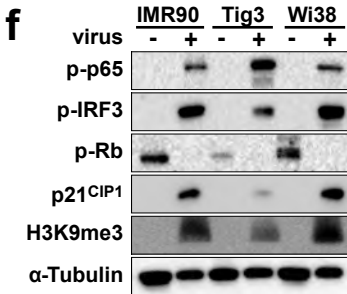
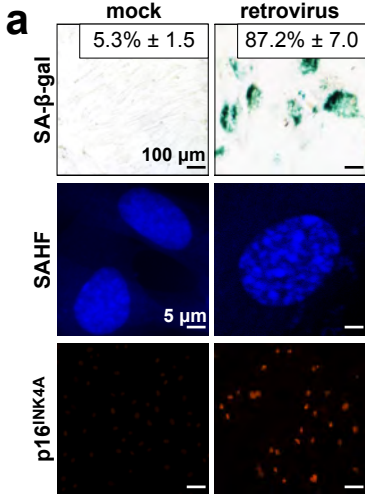
1236 ²Alveolar damage is the average of alveolar epithelial necrosis and alveolar edema.

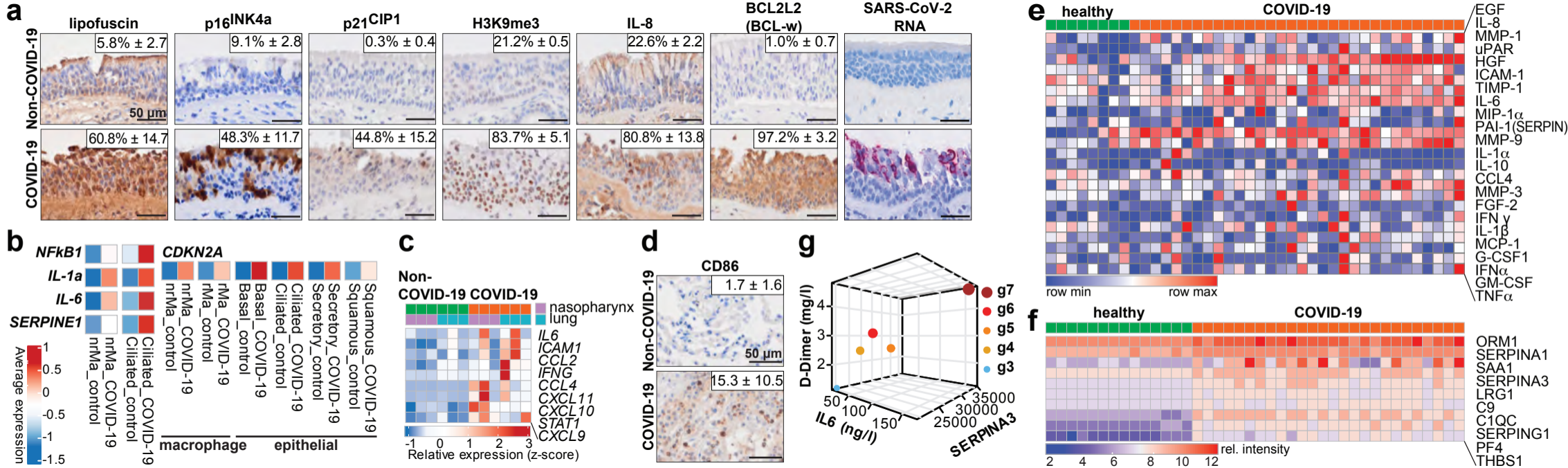
1237 ³Endothelial damage is the average of endothelialitis and endothelial activation

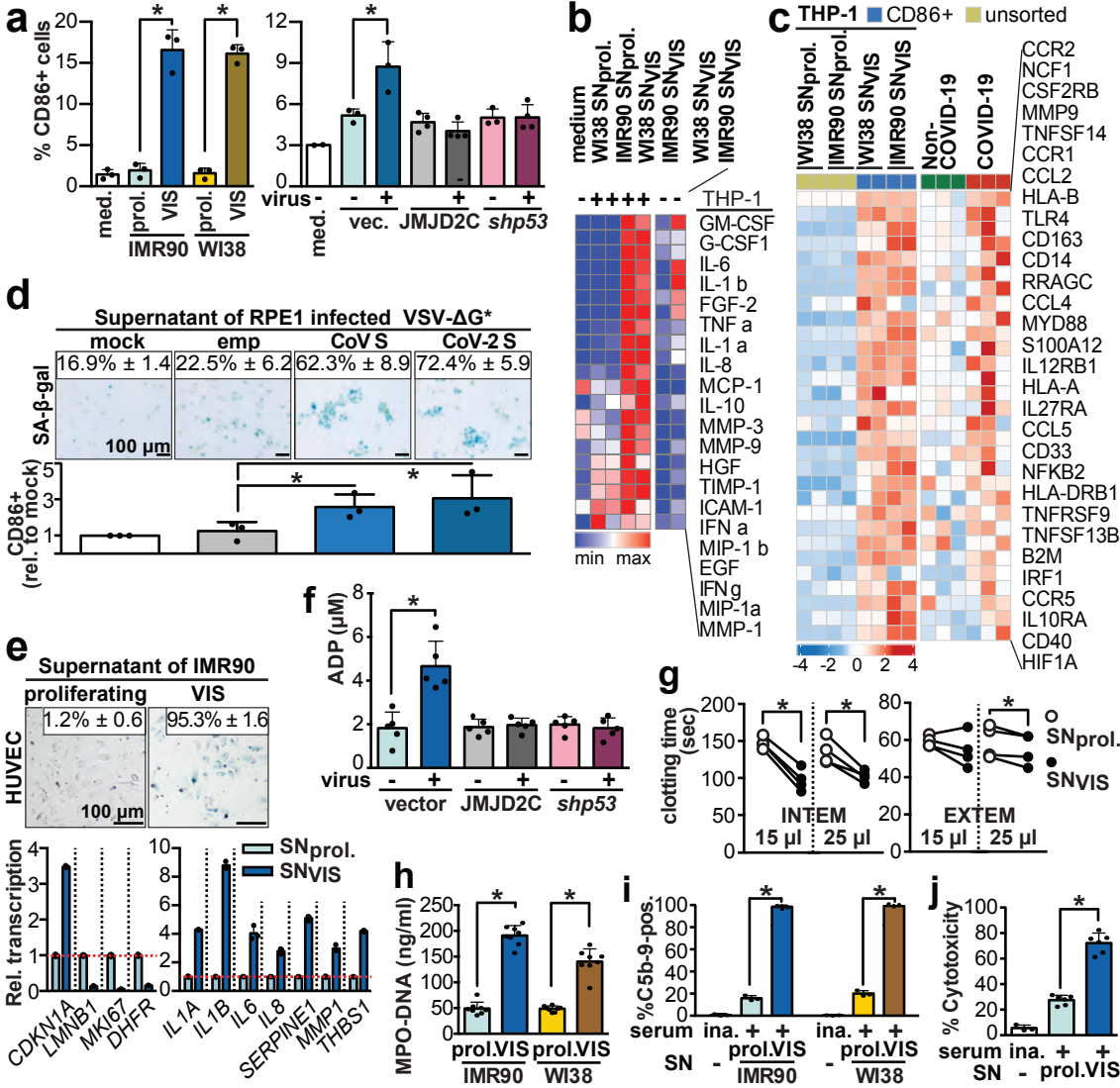
1238

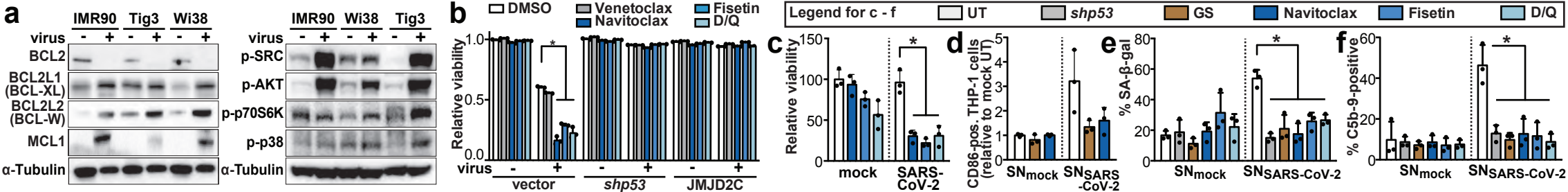
1239 **Extended Data Table 2 | Input data for Figure 5f.** Treatment, sex, age, symptoms, CRP,
1240 LDH, RT-PCR were collectively analyzed in a multi-variant analysis by agglomerative
1241 hierarchical clustering underlying the constellation plots.

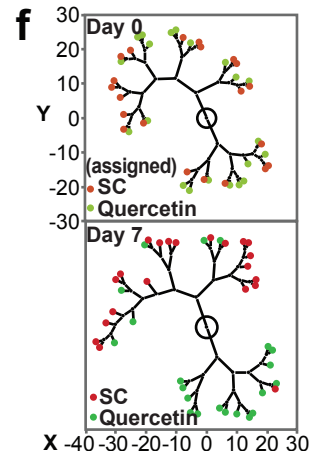
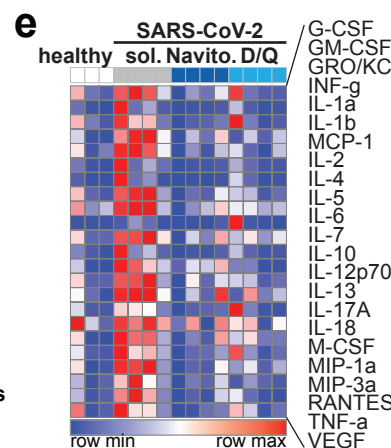
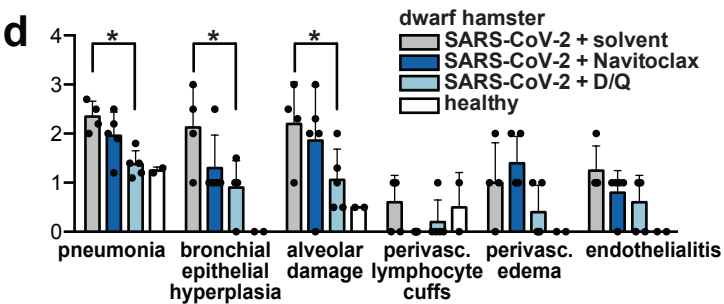
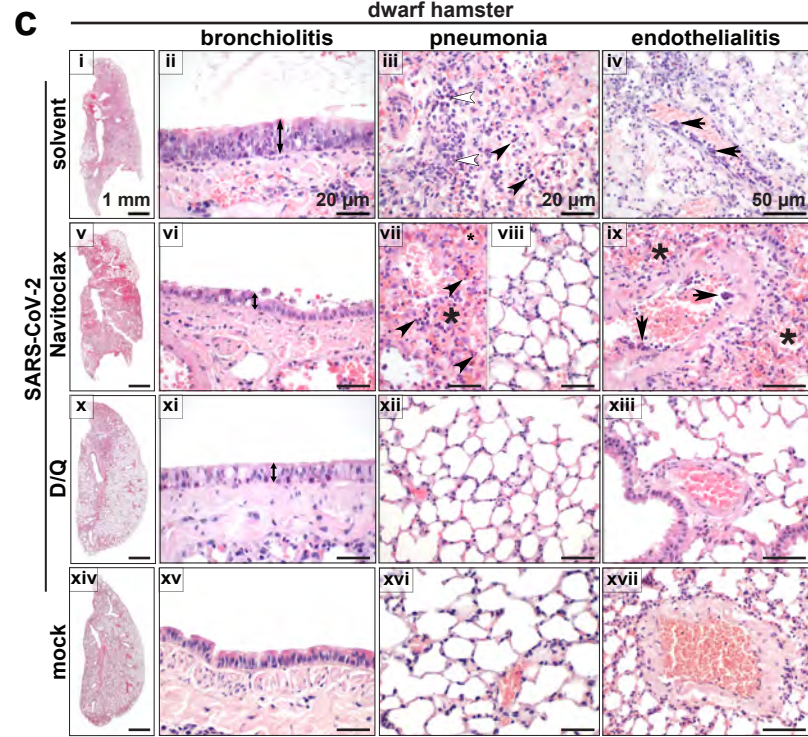
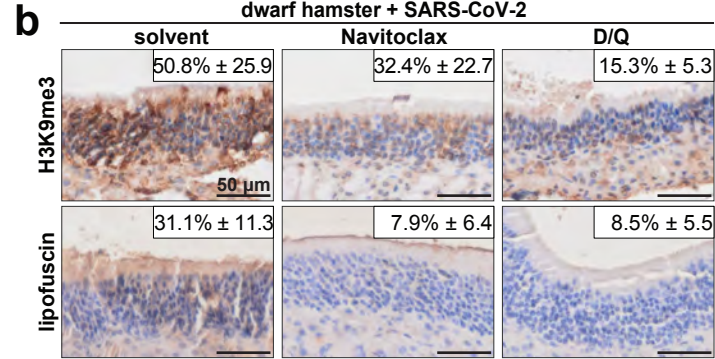
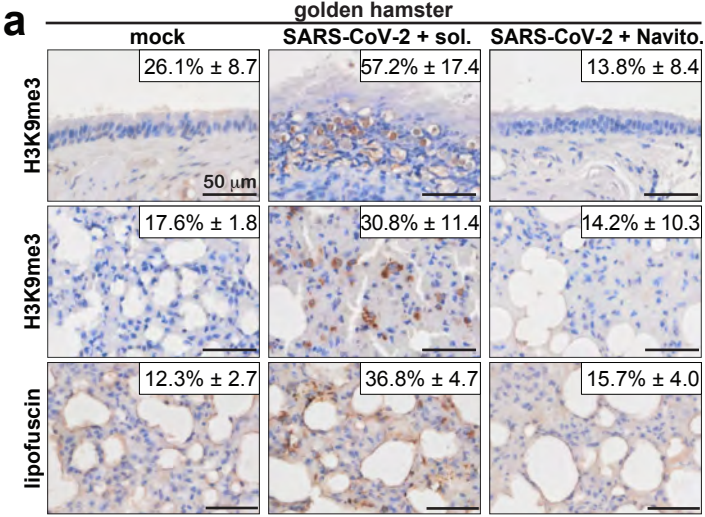
1242

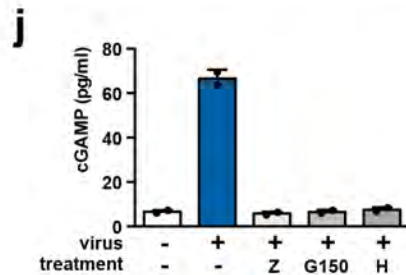
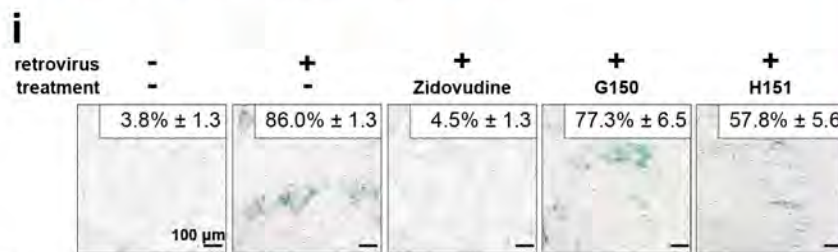
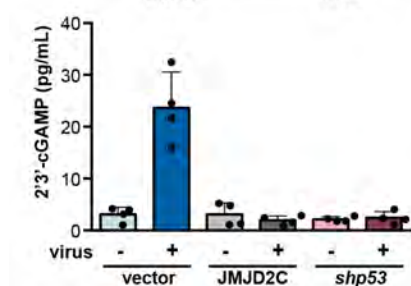
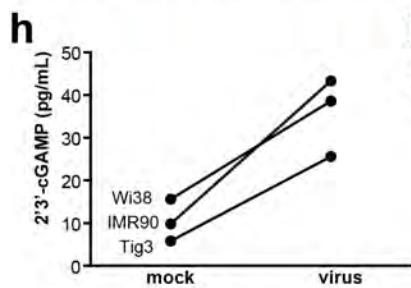
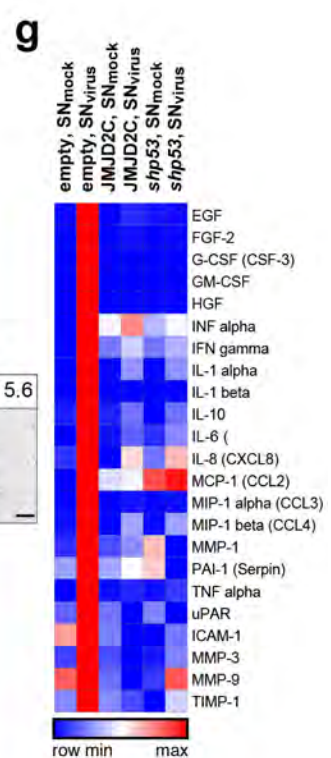
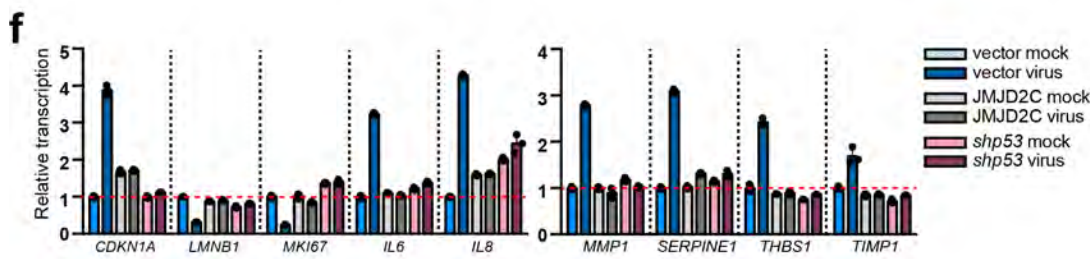
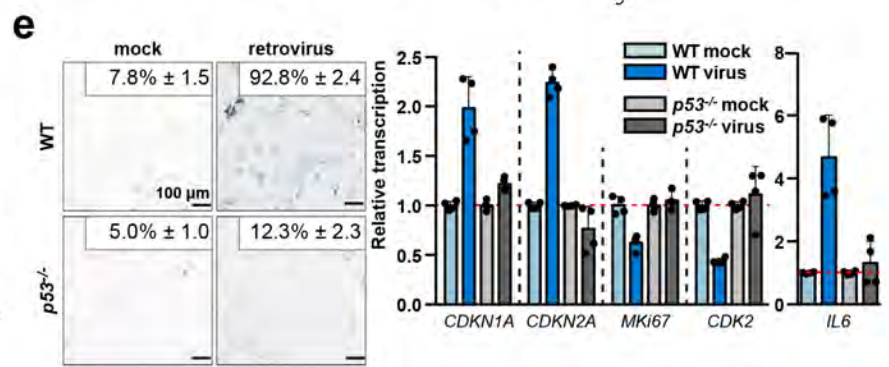
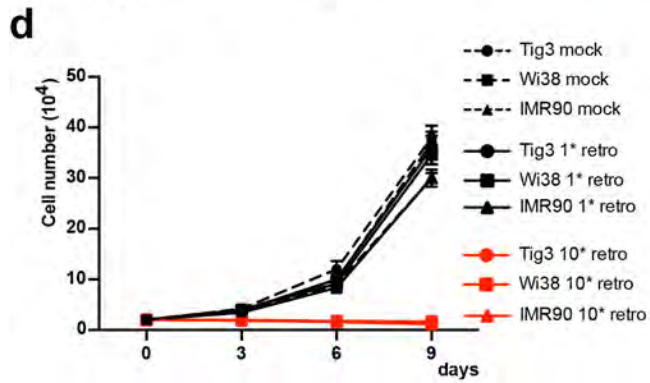
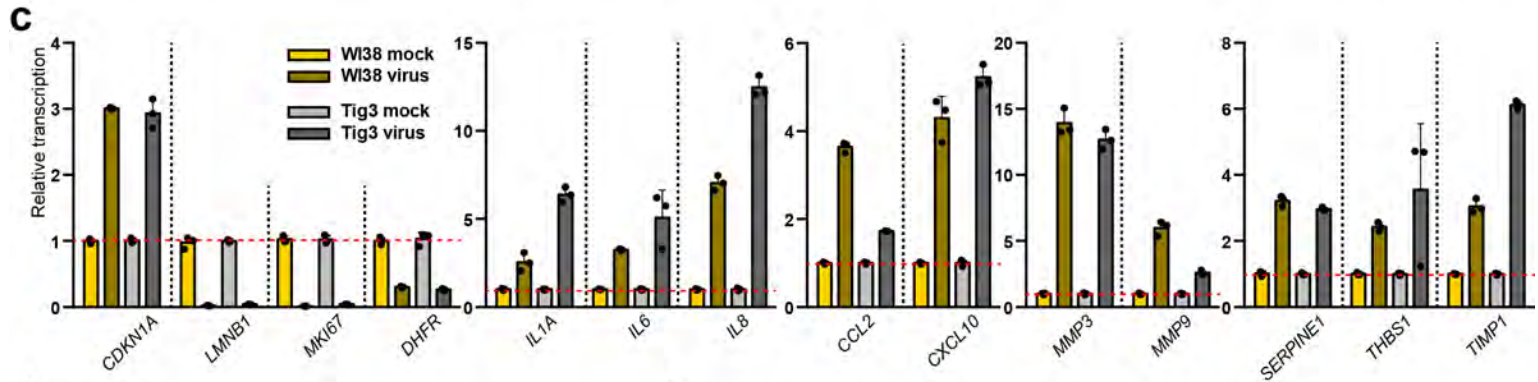
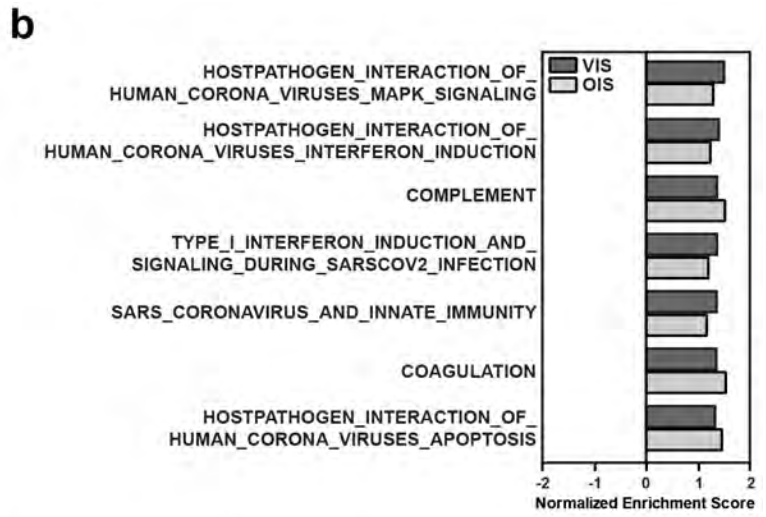
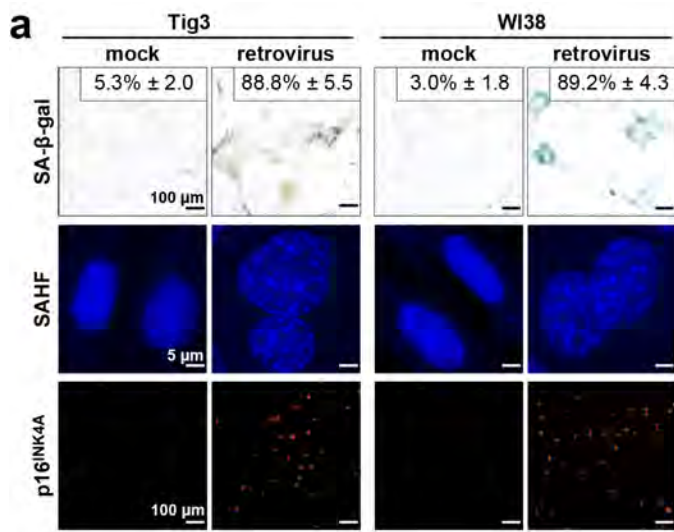


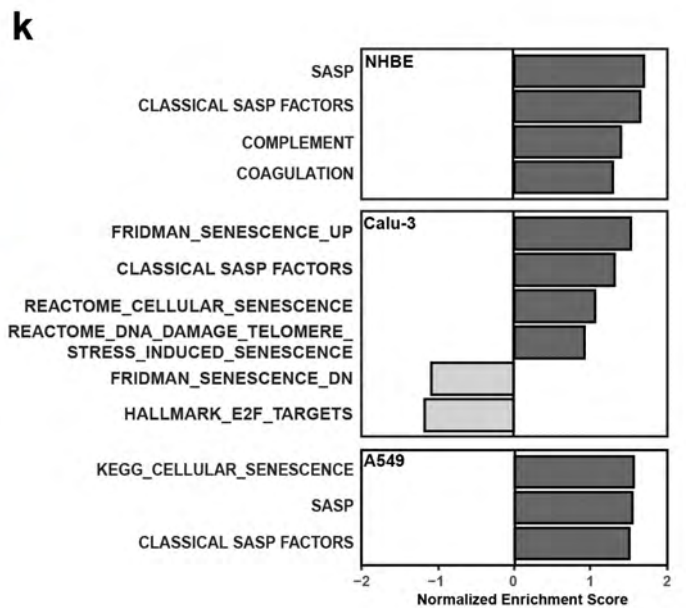
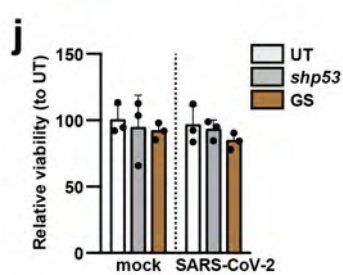
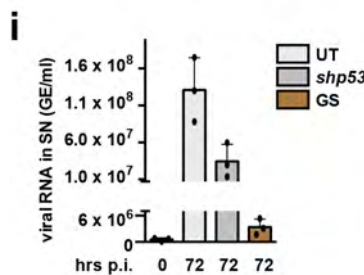
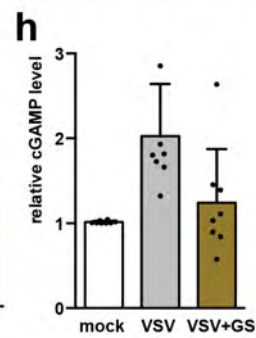
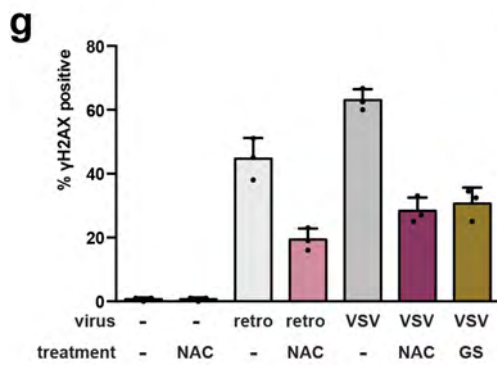
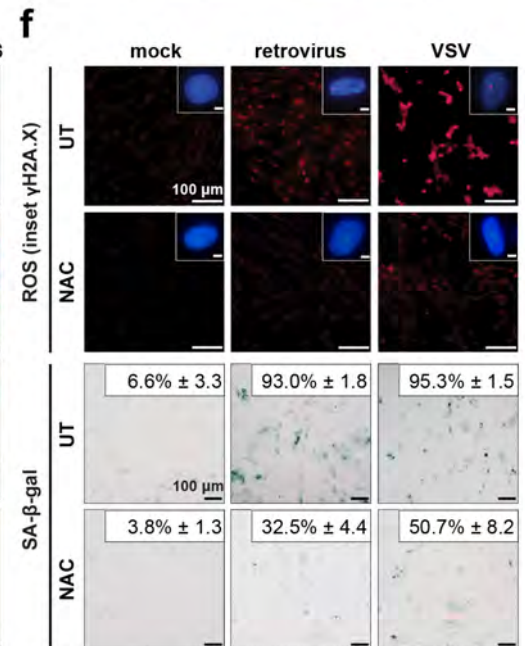
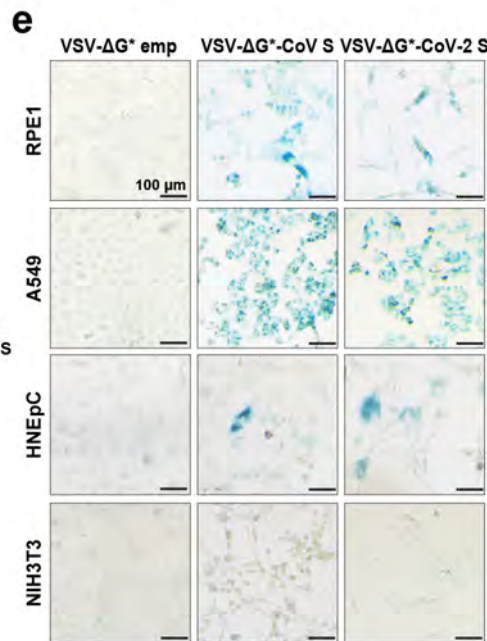
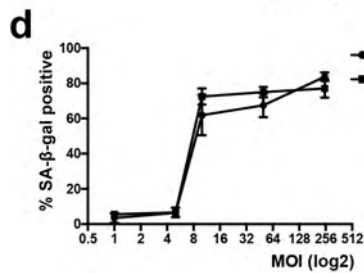
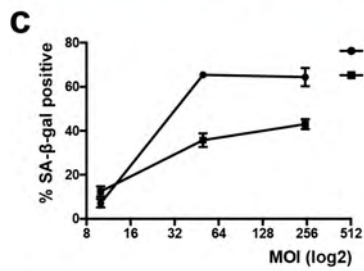
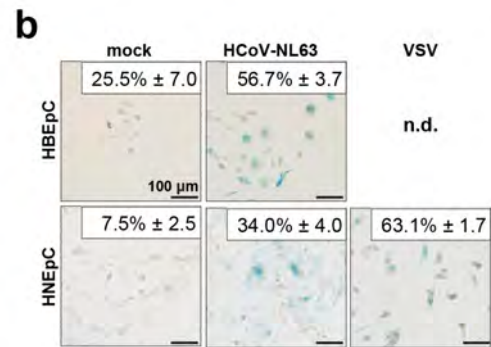
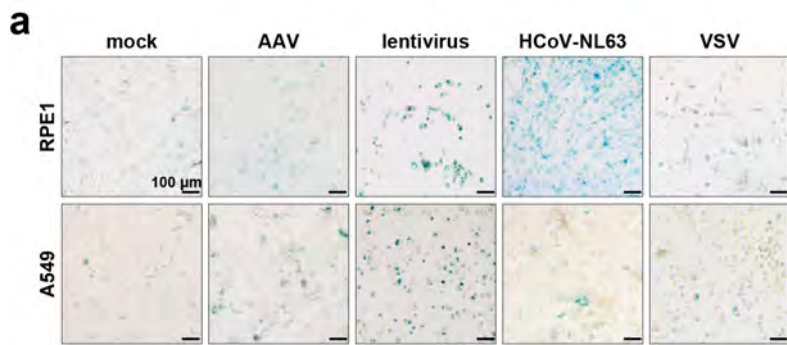


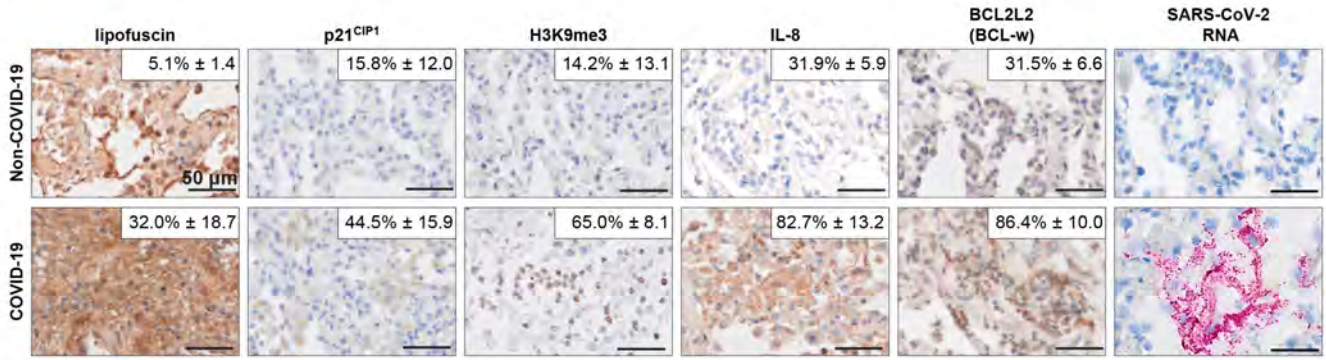
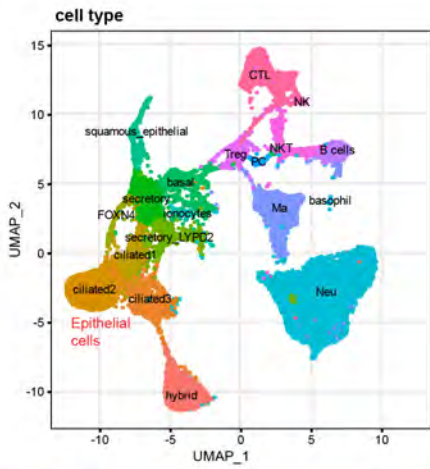
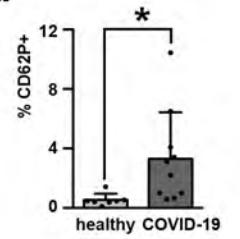
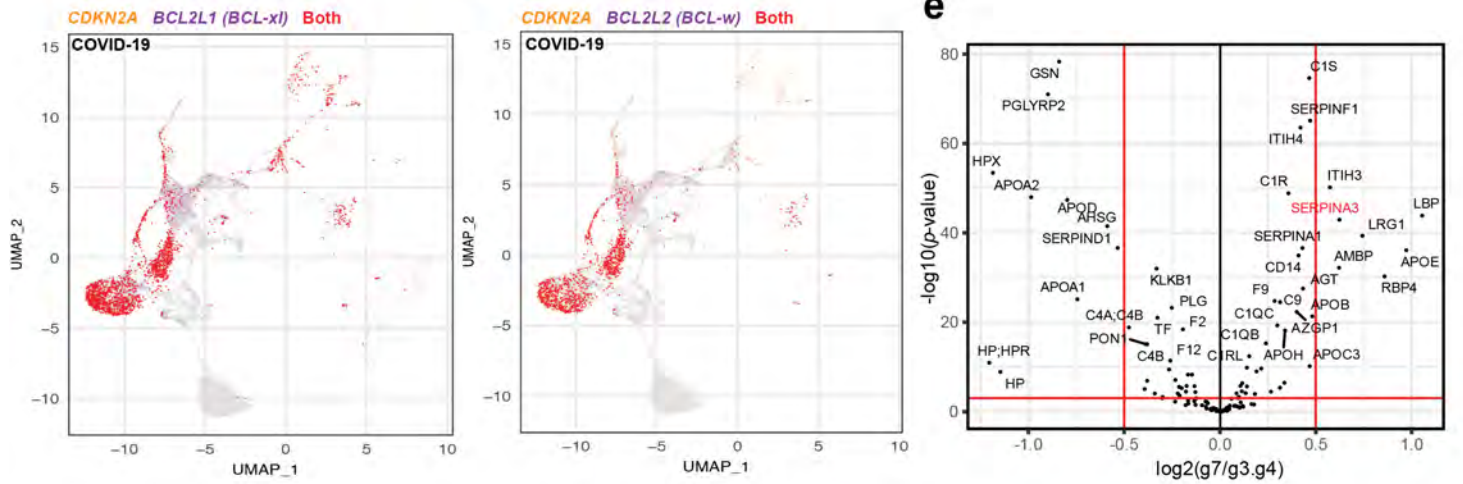
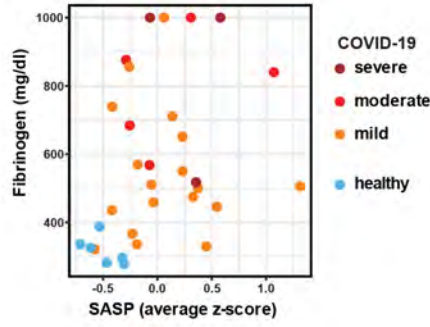
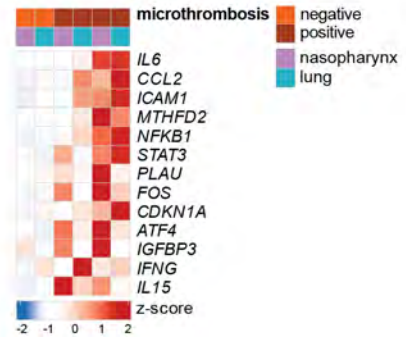
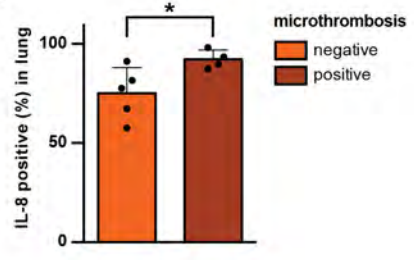


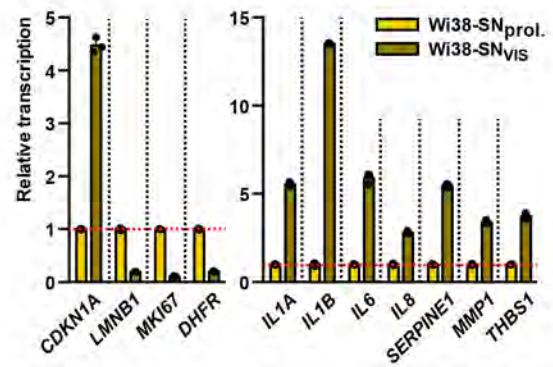
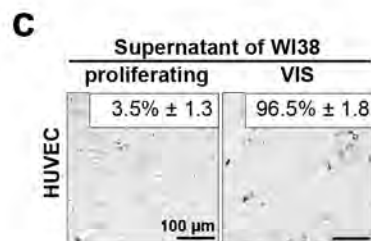
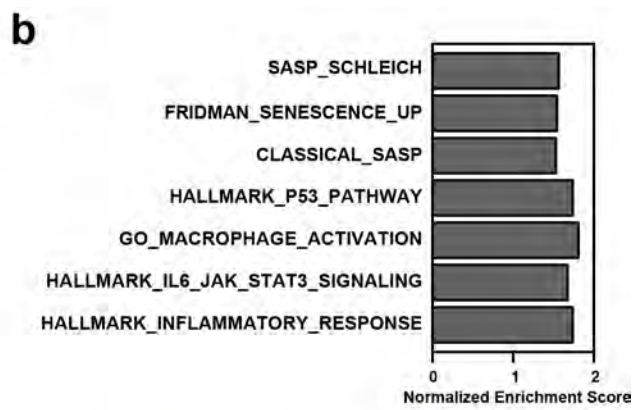
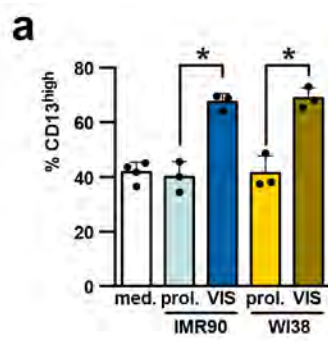


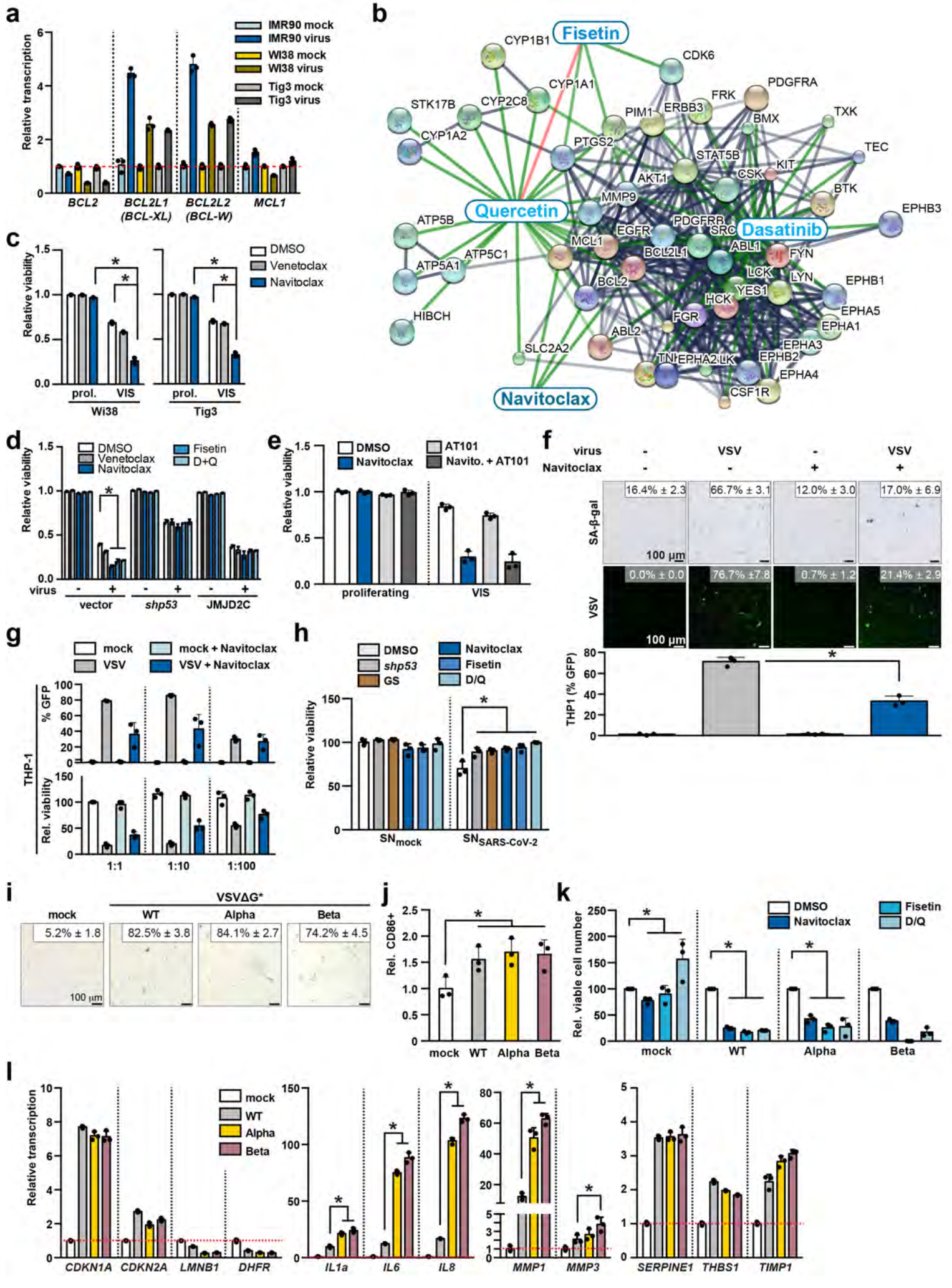


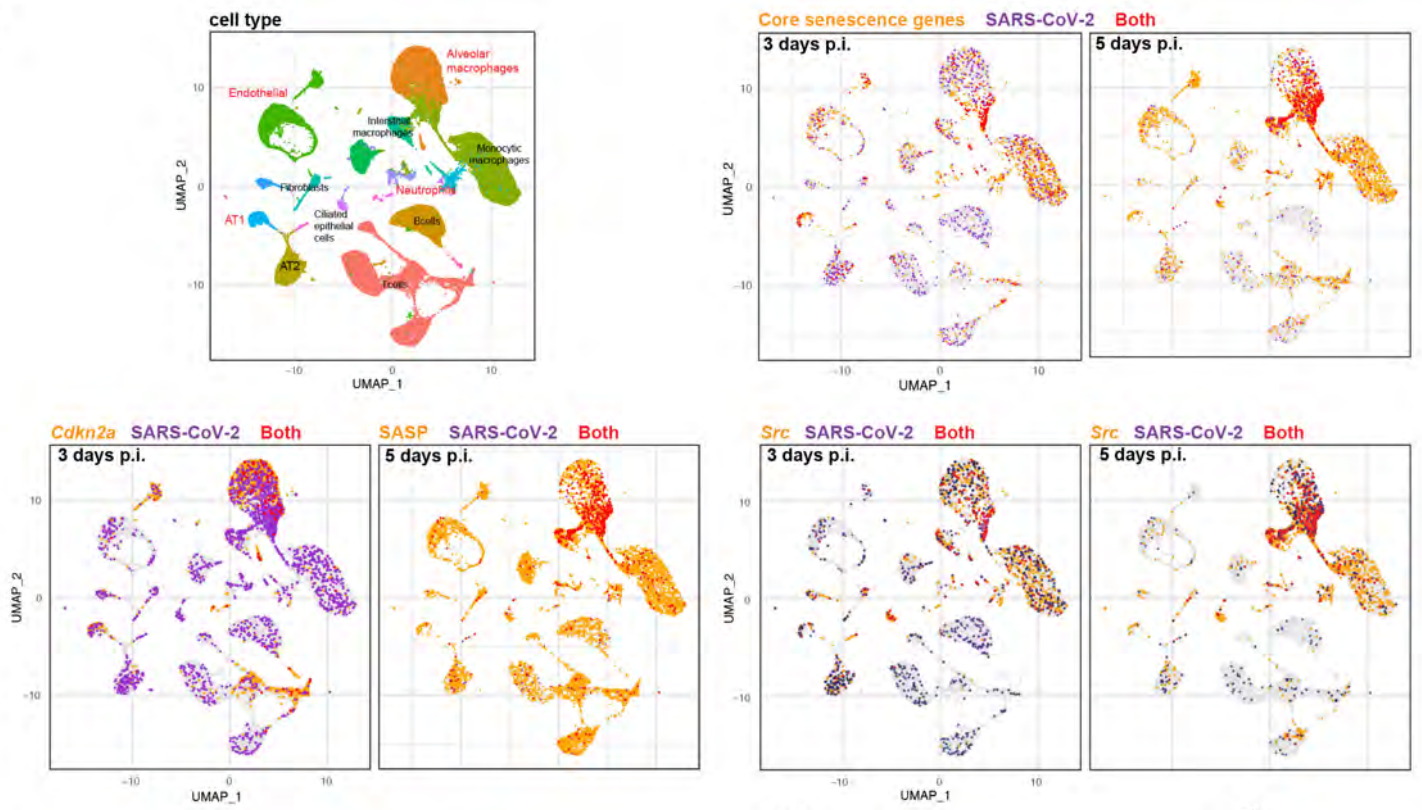
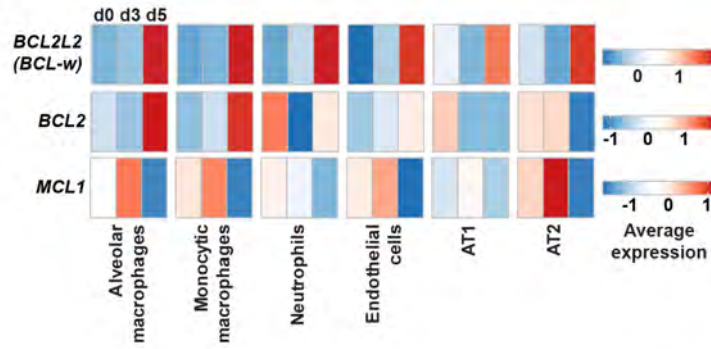
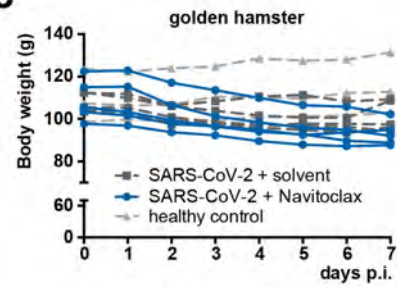
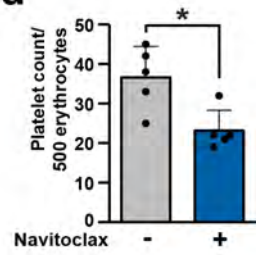
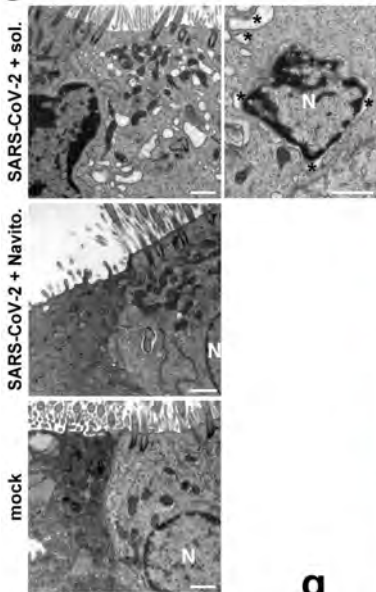
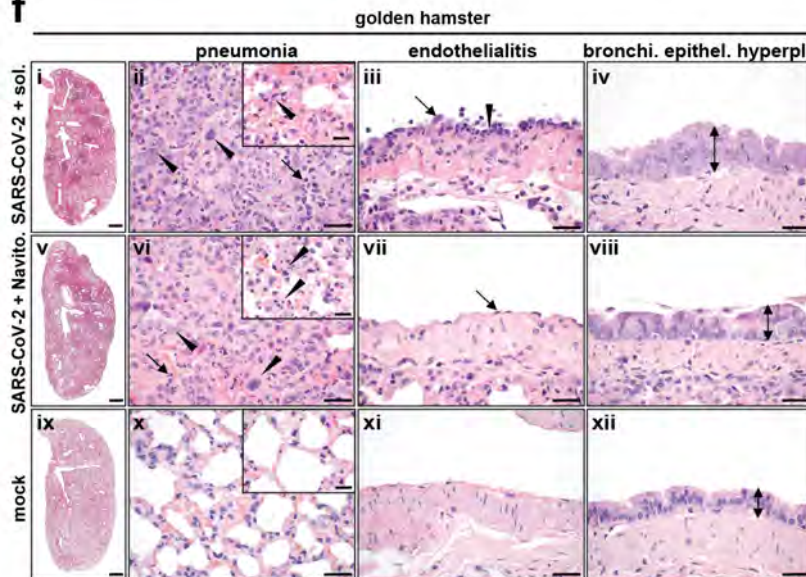
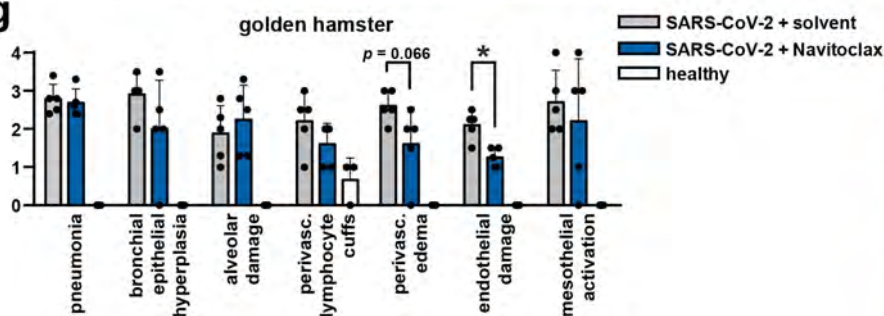
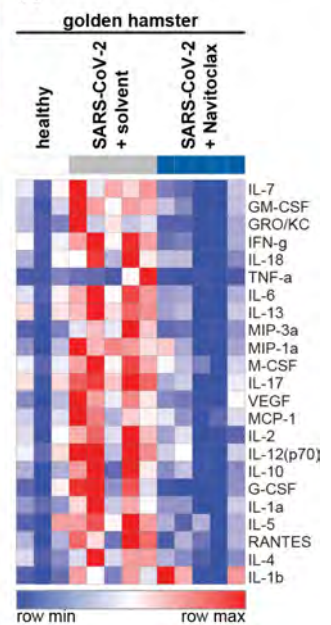


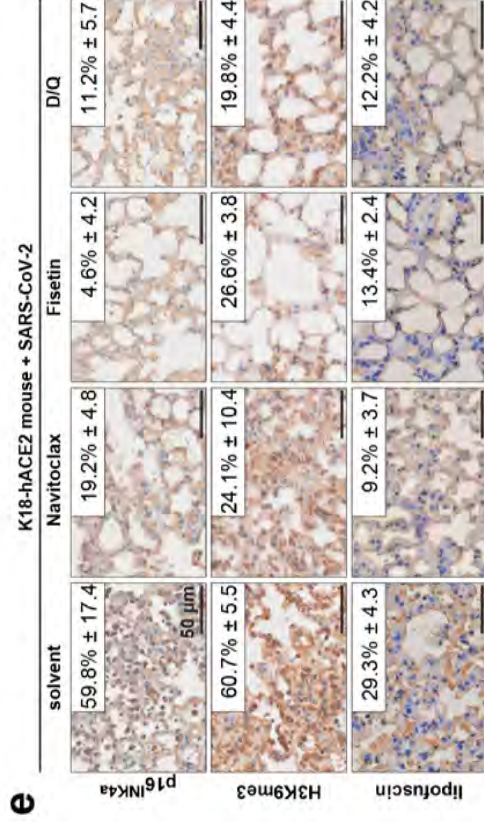
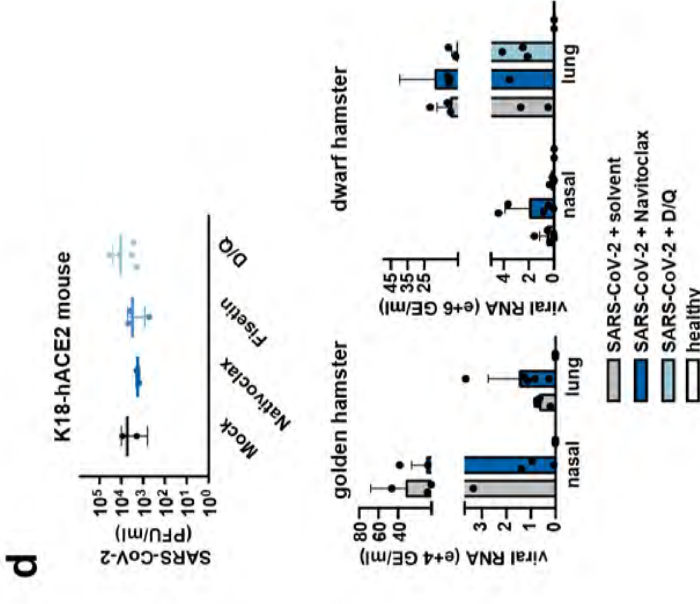
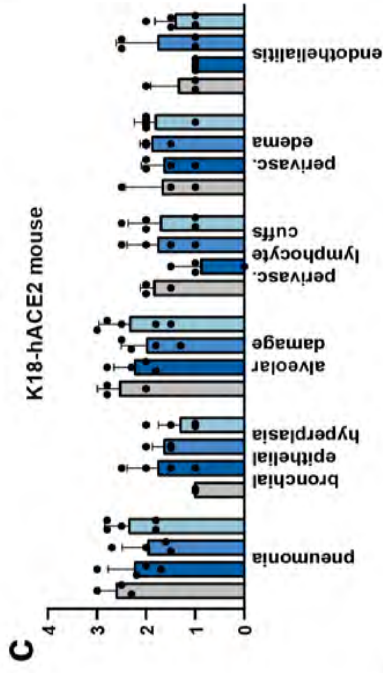
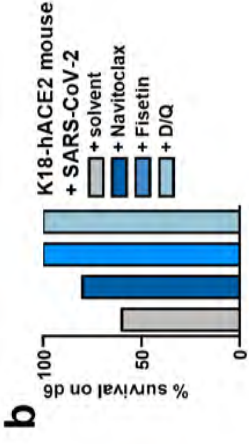
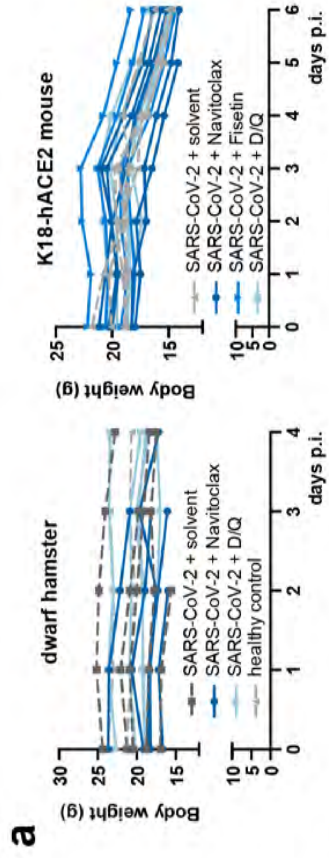


a**b****c****d****e****f****g****h**



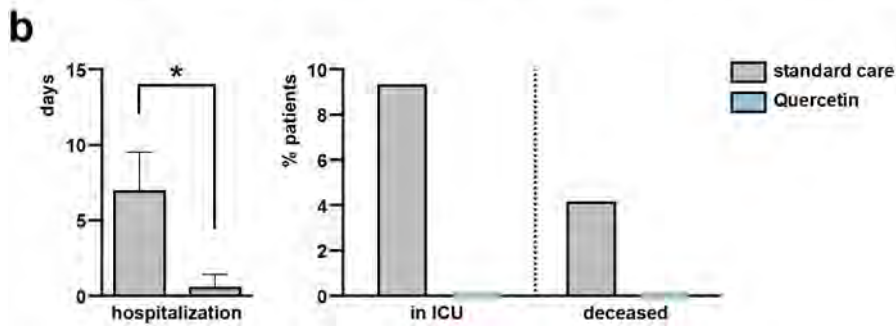


a**b****c****d****e****f****g****h**



a

		Frequency: Hospitalization					Frequency: Need of oxygen		
		N	Y				N	Y	
Quercetin					Quercetin				
SC					SC				
$p = 0.0024$	Odds Ratio (SC/Q)		Lower 95%	Upper 95%	$p = 0.0002$	Odds Ratio (SC/Q)	Lower 95%	Upper 95%	
		3.996	1.624	9.831		18.963	2.461	146.101	



Animal Nr.	Infection	Treatment	Time (dpi)	Pneumonia					Pneumonia score ¹	Bronchial epithelial necrosis	Bronchial inflammation	Bronchial epithelial hyperplasia	Alveolar epithelial necrosis	Alveolar edema	Alveolar damage ²	Perivascular edema	Perivascular lymphocytic cuffing	Hyperplasia ATII	Endothelialitis
				% affected score*	Degree of inflammation**	Lymphocytes	Macrophages	Neutrophils											
ND/Q_1	SARS-CoV-2	solvent	4	3	2-3	2	3	2	2.5	1-2	2	2	2-3	2-3	2.5	1	1	1-2	1
ND/Q_2	SARS-CoV-2	solvent	4	4	3	1	2-3	3	2.7	2-3	2	2-3	3	3	3.0	2	0	1	2
ND/Q_3	SARS-CoV-2	solvent	4	0	1	1	1	1	1.0	0	0	0	0	0.0	0	1	0	0	
ND/Q_4	SARS-CoV-2	solvent	2	3	2	1-2	2	1-2	2.0	2	2	1	1	1.0	0	1	1	1	
ND/Q_5	SARS-CoV-2	solvent	3	3	2-3	1	2	2-3	2.2	1-2	2	3	2-3	2	2.3	1-2	0	0	1
ND/Q_6	SARS-CoV-2	navitoclax	4	1	1	1	2	1	1.2	1	1	1	0	0.0	1	0	0	0	
ND/Q_7	SARS-CoV-2	navitoclax	3	4	3	1	2-3	2	2.5	2	1	2-3	3	3	3.0	2	0	1	1
ND/Q_8	SARS-CoV-2	navitoclax	3	2	2	1	2	2	2.0	3	1	1	2	2	2.0	2	0	1	1
ND/Q_9	SARS-CoV-2	navitoclax	2	2	2-3	1	2	2	1.9	3	1-2	1	2	2	2.0	1	0	1	1-2
ND/Q_10	SARS-CoV-2	navitoclax	3	3	2-3	1	2-3	2	2.2	3	1	1	2	2-3	2.3	1	0	1	1
ND/Q_11	SARS-CoV-2	D/Q	4	0	1	1	2	1	1.2	0	0	0	0	1	0.5	0	0	0	1
ND/Q_12	SARS-CoV-2	D/Q	4	1	1	1	1-2	1	1.1	0	1	1	0	1	0.5	0	0	0	0
ND/Q_13	SARS-CoV-2	D/Q	4	2	1	1	1-2	1-2	1.4	1	1	1	1	1-2	1.3	1	0	0	1
ND/Q_14	SARS-CoV-2	D/Q	4	2	1	1	2	1	1.4	1	1	1	1	1	1.0	0	0	0	0
ND/Q_15	SARS-CoV-2	D/Q	4	2	2	1	2	2	1.8	2	1	1-2	2	2	2.0	1-2	1	1	1-2
ND/Q_16	mock	mock	4	0	1	1	2	1	1.2	0	0	0	0	1	0.5	0	0	0	0
ND/Q_17	mock	mock	4	0	1	1-2	2	1	1.3	0	0	0	0	1	0.5	0	1	0	0

Animal Nr.	Infection	Treatment	Time (dpi)	Pneumonia					Pneumonia score ¹	Bronchial epithelial necrosis	Bronchial inflammation	Bronchial epithelial hyperplasia	Alveolar epithelial necrosis	Alveolar edema	Alveolar damage ²	Perivascular edema	Perivascular lymphocytic cuffing	Hyperplasia ATII	Endothelialitis	Endothelial activation	Endothelial damage ³	Mesothelial activation
				% affected score*	Degree of inflammation**	Lymphocytes	Macrophages	Neutrophils														
NX1	SARS-CoV2	Navitoclax	7	2	2-3	3	2-3	2	2.4	0	1	2	2-3	0	1.3	2	2	3	0	2	1	3
NX2	SARS-CoV2	Navitoclax	7	3	2-3	3	2-3	2	2.6	0	0	3-4	3.5	2	2.8	1-2	1	4	0	3	1.5	4
NX3	SARS-CoV2	Navitoclax	7	2	2-3	2	2-3	3	2.4	0	2	2-3	2-3	0	1.3	0	1	2-3	0	2	1	1
NX4	SARS-CoV2	Navitoclax	7	2	3	2-3	3	3	2.7	0	1	2	3	2	2.5	2	2	3-4	0	3	1.5	0
NX5	SARS-CoV2	Navitoclax	7	3	4	3	3-4	3	3.3	0	0	0	4	2-3	3.3	2-3	2	4	0	2-3	1.25	3
NX6	SARS-CoV2	solvent	7	2	3	3	3	3	2.8	0	1	3	3	2-3	2.8	2-3	2	3	1-2	3	2.25	2-3
NX7	SARS-CoV2	solvent	7	2	2-3	3	2-3	2-3	2.5	0	0	3	2	0	1.0	2-3	2-3	3	0	3	1.5	3
NX8	SARS-CoV2	solvent	7	2	3	3	3	3	2.8	0	0	2	2	2	2.0	3	1	3-4	1-2	3	2.25	2
NX9	SARS-CoV2	solvent	7	3	4	4	3-4	2-3	3.4	0	0	3-4	2	2-3	2.3	3	3	4	2	3	2.5	4
NX10	SARS-CoV2	solvent	7	1	2-3	3	2-3	3	2.4	0	0	3	2-3	0	1.3	2	2-3	3	1	3	2	2
NX11	mock	mock	7	0	0	0	0	0	0.0	0	0	0	0	0	0.0	0	0	0	0	0	0	0
NX12	mock	mock	7	0	0	0	0	0	0.0	0	0	0	0	0	0.0	0	1	0	0	0	0	0
NX13	mock	mock	7	0	0	0	0	0	0.0	0	0	0	0	0	0.0	0	1	0	0	0	0	0

Patient Nr.	Treatment	Sex	Gender code	Age (years)	CRP d1	CRP d7	CPR d7 - d1	LDH d1	LDH d7	LDH d7 - d1	Symptoms d7 - d1	RT-PCR d1	RT-PCR d7
1	Q	F	0	45	4,05	0,43	-3,62	240	190	-50	-3	Positive	Negative
2	Q	F	0	20	6,7	0,99	-5,71	341	230	-111	-2	Positive	Negative
3	Q	M	1	68	3,54	0,34	-3,2	298	240	-58	-2	Positive	Negative
4	Q	F	0	40	3	0,5	-2,5	220	140	-80	0	Positive	Negative
5	Q	M	1	29	10,2	1,5	-8,7	560	331	-229	-1	Positive	Negative
6	Q	F	0	32	19	0,75	-18,25	605	256	-349	-2	Positive	Negative
7	Q	M	1	38	0,42	0,41	-0,01	175	127	-48	-3	Positive	Negative
8	Q	M	1	30	1	1	0	300	202	-98	-2	Positive	Negative
9	Q	F	0	24	2,1	0,5	-1,6	402	264	-138	-2	Positive	Negative
10	Q	M	1	56	38	55	17	709	678	-31	-3	Positive	Positive
11	Q	F	0	53	5	1	-4	340	220	-120	-3	Positive	Negative
12	Q	M	1	70	37	46	9	300	309	9	-2	Positive	Positive
13	Q	F	0	66	15	3	-12	267	220	-47	-2	Positive	Negative
14	Q	M	1	30	24	5	-19	176	160	-16	-4	Positive	Negative
15	Q	F	0	32	16	21	5	250	274	24	-1	Positive	Positive
16	Q	F	0	34	67	3,1	-63,9	345	213	-132	-4	Positive	Negative
17	Q	M	1	43	45	10	-35	678	248	-430	-3	Positive	Negative
18	Q	M	1	38	60	25	-35	770	279	-491	-2	Positive	Negative
19	Q	F	0	45	80	27	-53	670	370	-300	-3	Positive	Negative
20	Q	F	0	47	75	30	-45	535	270	-265	-3	Positive	Positive
21	Q	M	1	52	60	25	-35	610	450	-160	-2	Positive	Positive
22	Standard	F	0	54	62	40	-22	352	320	-32	-2	Positive	Positive
23	Standard	F	0	56	80	77	-3	512	459	-53	-3	Positive	Positive
24	Standard	M	1	62	55	43	-12	323	310	-13	-3	Positive	Positive
25	Standard	F	0	45	66	48	-18	402	380	-22	-2	Positive	Positive
26	Standard	F	0	59	78	66	-12	612	551	-61	-3	Positive	Positive
27	Standard	M	1	95	17,14	12,2	-4,94	320	280	-40	-2	Positive	Positive
28	Standard	M	1	37	12,5	1,6	-10,9	262	257	-5	-3	Positive	Positive
29	Standard	F	0	33	7,3	2,3	-5	203	285	82	-1	Positive	Negative
30	Standard	F	0	73	16	3,3	-12,7	615	359	-256	-1	Positive	Positive
31	Standard	F	0	57	17,5	5	-12,5	267	231	-36	-2	Positive	Positive
32	Standard	M	1	72	73	5	-68	256	231	-25	-1	Positive	Positive
33	Standard	F	0	57	12	24	12	232	250	18	-2	Positive	Positive
34	Standard	M	1	60	34	11,4	-22,6	640	250	-390	-1	Positive	Positive
35	Standard	M	1	51	48,7	12	-36,7	305	259	-46	-2	Positive	Positive
36	Standard	M	1	73	15	6	-9	347	243	-104	-1	Positive	Positive
37	Standard	M	1	68	4,78	1	-3,78	573	433	-140	-2	Positive	Positive
38	Standard	M	1	50	0,9	0,5	-0,4	344	250	-94	-2	Positive	Positive
39	Standard	M	1	42	0,5	0,5	0	250	253	3	-3	Positive	Negative
40	Standard	F	1	69	5,51	6,2	0,69	358	745	387	-2	Positive	Positive
41	Standard	F	0	42	1	0,5	-0,5	240	320	80	-1	Positive	Positive
42	Standard	F	0	25	33,9	15,2	-18,7	250	214	-36	-2	Positive	Positive